

Petrogenesis, LA-ICP-MS zircon U-Pb geochronology and geodynamic implications of the Kribi metavolcanic rocks, Nyong Group, Congo craton

Hermine Mvodo¹ · Sylvestre Ganno¹  · Gus Djibril Kouankap Nono² ·

Donald Hermann Fossi^{1,3} · Philomene Estelle Nga Essomba^{1,4} ·

Marvine Nzepang Tankwa^{1,3} · Jean Paul Nzenti¹

Received: 6 September 2021 / Revised: 10 January 2022 / Accepted: 11 January 2022 / Published online: 31 March 2022

© The Author(s), under exclusive licence to Science Press and Institute of Geochemistry, CAS and Springer-Verlag GmbH Germany, part of Springer Nature 2022

Abstract Metavolcanic rocks are well-exposed in the Kribi area within the Nyong Group, Congo craton, but their origin, age, and tectonic significance are poorly known. Here we report integrated field mapping and petrography, geochemistry, and LA-ICP-MS zircon U-Pb ages of these metavolcanic rocks to constrain their petrogenesis and geodynamic implications. The studied rocks consist of mafic granulite, garnet-amphibole gneiss, and garnet-biotite gneiss, and occur interbanded with sharp contact and intruded by syenite dyke. These metavolcanic rocks are classified as MORB-like tholeiitic to calc-alkaline basalts, basaltic andesite, and rhyodacite rocks with within-plate setting geochemical signatures. The metabasite rocks (basalt to basaltic andesite protolith) are likely the equivalent of a spinel peridotite product representing $\sim 2\text{--}5\%$ partial melting of metasomatized mantle source, while the metarhyodacite rocks are derived from the fractional crystallization of the same parental magma. Zircon U-Pb data revealed that the rhyodacite rocks initially formed at 2671 ± 51 Ma and underwent later metamorphism at

2065 ± 55 Ma. The Neoarchean protolith age is comparable to the ca. 2628 Ma tholeiitic magmatism and ca. 2666 Ma high-K granites, suggesting bimodal Neoarchean magmatic event within the Ntem Complex, while the metamorphic ages fall within the ca. 2100–2000 Ma high-grade tectono-metamorphic event attributed to Eburnean/Trans-Amazonian orogeny. At the regional scale, metavolcanic rocks with similar origins and ages are documented in the São Francisco Craton in Brazil, suggesting comparable geodynamic evolution on both sides of the south Atlantic during the Paleoproterozoic.

Keywords Metavolcanic rocks · MORB · Within plate volcanic zone · Mantle source · Fractional crystallization · Congo craton · Cameroon

1 Introduction

Precambrian geodynamic processes aim at understanding the evolution throughout the time of the Earth's interior and surface. Many workers Taylor and McLennan 1985; Hoffmann et al. 2010; Gerya 2014 and references therein) have proposed diverse models for the Precambrian geodynamic processes such as plate tectonics, orogeny, subduction, collision, craton formation, and stability. Based on geochemical, petrological, and geochronological data, it becomes possible to constrain the main geodynamic processes which controlled the formation and preservation of Precambrian cratons (Hoffmann et al. 2010; Beuchert et al. 2010; Currie and Van Wijk 2016). For instance, Precambrian volcanic rocks which constitute the earliest manifestation of ancient igneous activity are considered to be extremely important for the understanding of mantle-crust

✉ Sylvestre Ganno
sganno2000@gmail.com

¹ Department of Earth Sciences, University of Yaoundé I, P.O. Box 812, Yaoundé, Cameroon

² Department of Geology, HTTC, University of Bamenda, P.O. Box 39, Bambili, Bamenda, Cameroon

³ Institute for Geological and Mining Research, P.O. Box 4110, Yaoundé, Cameroon

⁴ Faculty of Mines and Petroleum Industries, University of Maroua, Kaélé 08, Maroua, Cameroon

evolution Polat et al. 2000, 2002; Zhang et al. 2012b). Lack of preserved ancient volcanic rocks represent a fundamental barrier in improving the comprehension of how the Earth evolved, thus the scarcity of consensus and the persistence of intriguing and controversial issues regarding the Precambrian geodynamic processes Taylor and McLennan 1985; Hoffmann et al. 2010; Gerya 2014 and references therein).

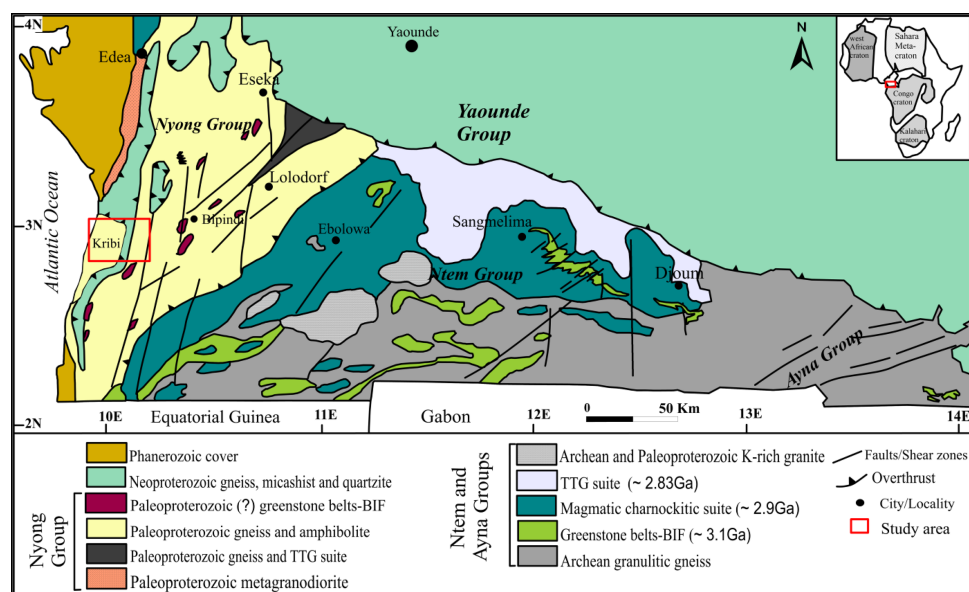
In Southern Cameroon, Precambrian metavolcanic rocks are reported within the Congo Craton (CC) represented by the Ntem Complex, which is characterized by a conspicuous presence of greenstones belt (Loose and Schenk 2018; Bouyo Houketchang et al. 2019; Fuanya et al. 2019; Moudioh et al. 2020; Nga Essomba et al. 2020; Kwamou et al. 2021). This belt trends E–W and extends over 500 km from Mbalam to the East to Kribi town to the West (Maurizot et al. 1986; Suh et al. 2008; Ganno et al. 2018). The Ntem Complex encompasses the Neoarchean-Paleoproterozoic Nyong Group to the west and the Archean Ntem Group to the east (Maurizot et al. 1986; Lerouge et al. 2006; Owona et al. 2021; Soh Tamehe et al. 2021). Pioneers studies (e.g. Maurizot et al. 1986; Feybesse et al. 1986, 1998) have revealed that the Nyong Group (Fig. 1) represents reactivated portion of the Archaean Congo craton throughout Eburnean/Trans-Amazonian and Pan-African/Braziliano orogenies, while other authors (e.g. Toteu et al. 1994; Penaye et al. 2004; Lerouge et al. 2006; Kankeu et al. 2018; Bouyo Houketchang et al. 2019; Nga Essomba et al. 2020) have propounded that the Nyong Group represents a Paleoproterozoic suture zone coeval to a nappe tectonic event between the Congo and São Francisco cratons. Furthermore, preserved fragments of this orogeny were reported in both NE Brazil and West Africa

(Ledru et al. 1989; Barbosa and Barbosa 2017). The Nyong Group consists of metamorphosed volcano-sedimentary rocks intruded by plutonic bodies. Previous geochronological studies of this group have revealed the Paleoproterozoic magmatic-metamorphic events, suggesting that the Nyong Group represents a reworked segment of the Archean Ntem Complex formed during the Eburnean/Trans-Amazonian orogeny (Nedelec et al. 1993; Toteu et al. 1994; Penaye et al. 2004; Lerouge et al. 2006; Ndema Mbongue et al. 2014; Owona et al. 2020a, 2021a). Moreover, recent studies (e.g. Loose and Schenk 2018; Bouyo Houketchang et al. 2019; Nga Essomba Tsoungui et al. 2020, and references therein) have revealed the occurrence of 2.09 Ga eclogites and serpentinites in this group, suggesting that the modern plate tectonic model has played a key role in the collision between the Congo and São Francisco craton.

The Kribi area is located to the western edge of the Nyong Group (Fig. 1), which comprises well-exposed metavolcanic rocks cropping out along the beach (Atlantic coast). The occurrence of these metavolcanic rocks is essential to determine the source and evolution of mafic magma in the Ntem Complex, thus improving the understanding of the formation and evolution of the Congo Craton. Furthermore, the location of the Kribi area within the CC could represent an important asset for the reconstruction of Gondwana since Congo – São Francisco cratons were likely linked by Mid-Ediacaran times.

In this contribution, we performed whole-rock geochemical and LA-ICP-MS U-Pb zircon analyses of these metavolcanic rocks in order (1) to constrain their sources and petrogenesis, (2) to determine their crystallization and metamorphic ages, and (3) to better understand Early

Fig. 1 Geological map of Southwestern Cameroon highlighting the Ntem Complex with the location of the studied area (red square) in the Nyong Group (adapted after Maurizot et al. 1986). The inset map shows the position of the Ntem Complex relative to the Congo Craton and other cratons in Africa



Precambrian geodynamic processes in the CC in this region and the whole Nyong group.

2 Geological setting

2.1 Regional geology

The Kribi area (Figs. 1 and 2) belongs to the Ntem Complex which represents the northwestern extension of the Congo Craton in the southern part of Cameroon (Maurizot et al. 1986; Nédélec et al. 1990; Pouclet et al. 2007). This complex is made up of two main lithological groups, namely the Nyong and Ntem Groups. The Nyong group comprises of tonalite–trondhjemite–granodiorite (TTG), dolerites, alkaline syenites, greenstone belts (epidosites, serpentinites), orthopyroxene–garnet gneisses (charnockites), garnet–amphibole–pyroxenites, biotite hornblende gneisses, banded iron formations (BIFs) and various monzonitic and magnetite bearing rocks (Lerouge et al. 2006; Ganno et al. 2015, 2017; Chombong et al. 2017; Nga Essomba et al. 2020). In the vicinity of the Kribi area, Neoproterozoic syenitic plutons occur in the ‘Mont des éléphants’, Ebondja, and Rocher du Loup areas (Toteu et al. 1994; Lerouge et al. 2006; Nsifa et al. 2013).

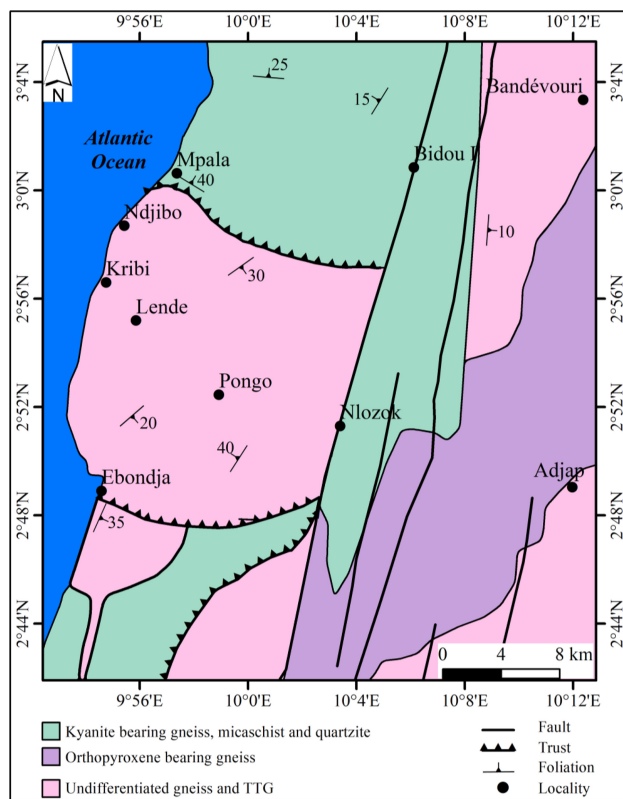


Fig. 2 Geological map of Kribi area (adapted from Kankeu et al. 2018)

Paleoproterozoic (2066 ± 4 Ma) granodiorites were reported at the Bonguen area, some 60 km North of Kribi (Lerouge et al. 2006). Kwamou et al. (2021) have recently documented 2050 Ma metavolcanic rocks (amphibolites) occurring as layers and/or discontinuous pods associated with BIFs at the Mewongo area located some 40 km to the Southeast of Kribi. The protolith of these amphibolites has a MORB composition, formed in an island arc geotectonic setting, and belongs to tholeiitic magma series generated from the partial melting of upper mantle at the shallow depth in spinel peridotite stability field. Studies focusing on eclogites and serpentinized peridotites (Loose and Schenk 2018; Bouyo Houketchang et al. 2019; Nga Essomba et al. 2020) reported not only a subduction-related environment within the Nyong Group but also that the subduction played during Paleoproterozoic as revealed by the SHRIMP zircon U-Pb eclogite facies metamorphism age of 2093 ± 45 Ma (Loose and Schenk 2018).

Recent geochronological studies of detrital zircons from BIFs constrained the maximum depositional age of the Nyong Group at 2422 ± 50 Ma (Soh Tamehe et al. 2021) or 2466 ± 62 Ma (Djoukouo Soh et al. 2021), while Owona et al. (2021a, b) bracketed the deposition of the Nyong Group between 2.4 and 2.2 Ga. High-grade metamorphism is widespread within the Nyong Group, coeval with tectonic emplacement of plutonic rocks (Toteu et al. 1994; Lerouge et al. 2006; Owona et al. 2020b), whereas the aforementioned Archaean to Paleoproterozoic metasedimentary and metaigneous rocks have also recorded Neoproterozoic imprints at ca. 600 Ma (Penaye et al. 1993; Toteu et al. 1994, 2006; Chombong et al. 2017; Nzepang Tankwa et al. 2021; Owona et al. 2021a), interpreted as the Pan-African disturbance event.

2.2 Local geology

Very few studies have been done in the Kribi area (e.g. Lerouge et al. 2006; Nsifa et al. 2013; Kankeu et al. 2018; Owona et al. 2021a). From the available literature, this part of the Atlantic coast in Cameroon comprises various ortho- and paragneisses, intruded by Pan-African metasyenite (Fig. 2). Outcrops of quartzite, BIF, and charnockite are also exposed in this part of Cameroon (Toteu et al. 1994; Lerouge et al. 2006; Teutsong et al. 2020). Recent works by Owona et al. (2021a, b) have documented high-grade metasedimentary rocks in the Kribi area. The LA-ICP-MS U-Pb zircon dating of these metasedimentary rocks revealed predominantly igneous zircon populations at ~ 2.7 and 2.4 Ga, overprinted by ~ 2.0 and 0.65 Ga metamorphic events. Structurally, the Kribi area has experienced three phases of deformation. The early planar fabric (S_1) was overprinted during D_2 folding under relatively high-T conditions, and subsequent D_3 wrenching

(Kankeu et al. 2018). The NNE-SSW trending Kribi-Campo shear zone (KCSZ) affected both older basement rocks and Pan-African high-grade metasediments.

3 Analytical methods

3.1 Petrography and whole-rock geochemistry

Fresh representative samples including seven mafic granulites, five garnet-amphibole gneiss, and five garnet-biotite gneiss were collected from different outcrops in the study area. Twenty-five polished thin sections were performed at Geotech Lab, Vancouver (Canada) on representative samples, and the microscopic studies were carried out at the Department of Earth Sciences, University of Yaoundé I (Cameroon). After careful petrographic examination, seventeen samples were selected for major, trace, and rare earth elements at Bureau Veritas Commodities Limited at Vancouver (Canada) using the inductively coupled plasma mass spectrometry (ICP-MS) method. The samples were pulverized to obtain a homogeneous sample out of which 0.2 g of rock powder was fused with 0.9 g LiBO₂ at 1000 °C, and then dissolved with 100 mm³ of HNO₃ at 4 %. Analytical uncertainties vary from 0.1 to 0.04 % for major elements, 0.1 to 0.5 % for trace elements; and 0.01 to 0.5 ppm for rare earth elements (REE). Analytical accuracy for REE is estimated at 5 % for concentrations > 10 ppm and 1 % when lower. Loss on ignition (LOI) was determined by weight difference after ignition at 1000 °C. Different standards were used and data quality assurance was established by applying these standards as unknown between samples.

3.2 Zircon U-Pb dating

LA-ICP-MS Zircon U-Pb geochronology was performed on one garnet gneiss (metarhyodacite rocks) sample (KR3). Zircon grains were extracted by heavy liquid and magnetic separation at the Langfang Rock Detection Technology Services Ltd in Hebei (China), before being handpicked under a binocular microscope for mounting in epoxy resin. To identify their internal structure and to choose potential target sites for the U-Pb analyses, cathodoluminescence (CL) images were obtained using a scanning electron microscope at the Institute of Geology and Geophysics, Chinese Academy of Sciences in Beijing. Measurements of U, Th, and Pb isotopes were conducted using an ESI NWR 193 nm laser ablation system and an AnalytikJena PQMS Elite ICP-MS instrument. GJ-1 and Plešovice were treated as quality control for geochronology. Operational and analytical methods are detailed by Hou et al. (2009). Measured compositions were corrected for common Pb

using non-radiogenic ²⁰⁴Pb. As corrections were sufficiently small to be insensitive to the choice of common Pb composition, an average of present-day crustal composition (Stacey and Kramers 1975) was used for common Pb, assuming that it is largely related to surface contamination introduced during sample preparation. Uncertainties relating to individual analysis in the data tables are reported at a δ level and mean ages for pooled U/Pb (and Pb/Pb) analyses are quoted at a 95 % confidence interval. Data reduction was conducted using the Isoplot/Ex v. 3.75 program (Ludwig 2003).

4 Results

4.1 Petrography

4.1.1 Mafic granulite

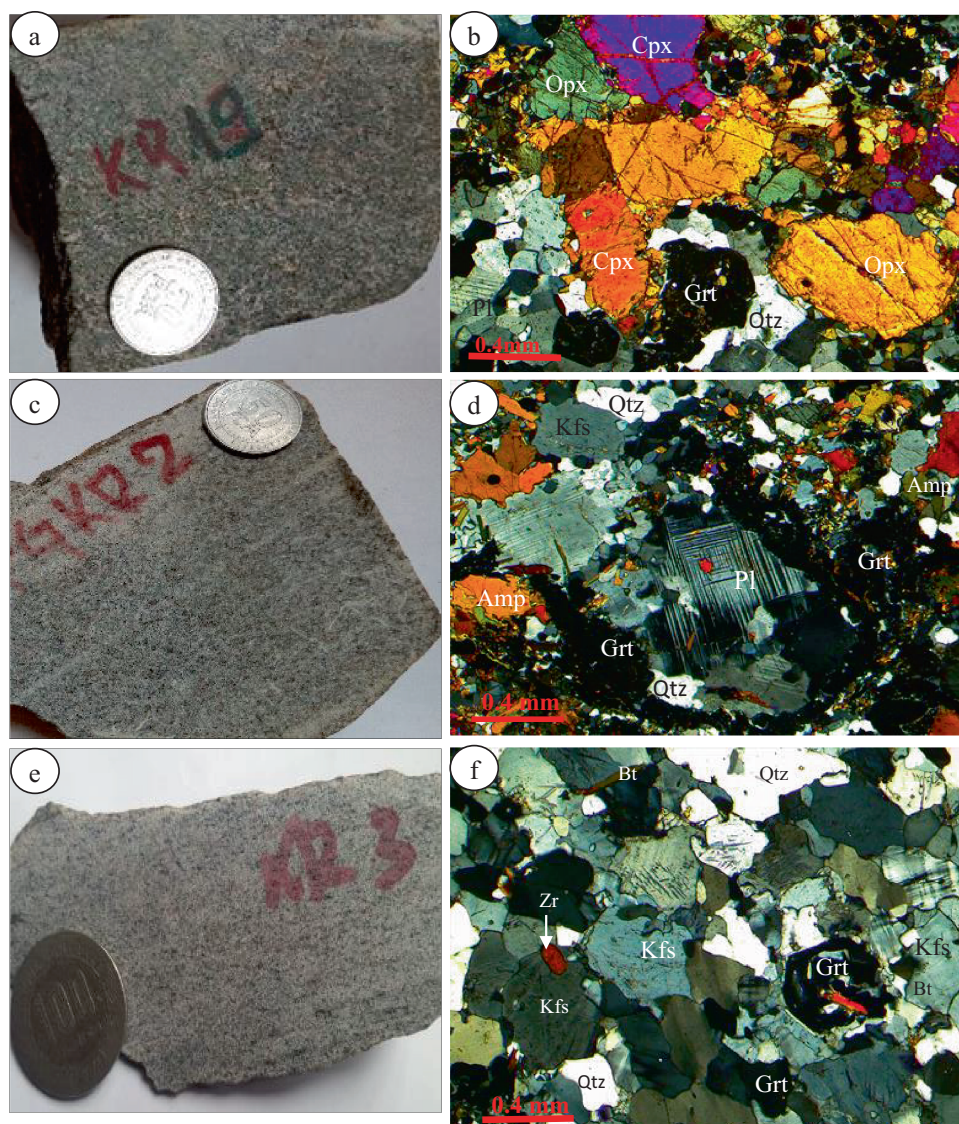
The mafic granulite is interbanded with garnet-amphibole gneiss and garnet-biotite gneiss, both of which are intruded by syenite dyke (Fig. 3a, b). In the hand specimen, the rock is dark grey in color and fine- to medium-grained, with a gneissose structure (Fig. 4a); whereas under the microscope, it displays a granoblastic heterogranular texture (Fig. 4b). Mineral assemblage consists of orthopyroxene + clinopyroxene + garnet + quartz + plagioclase, consistent with granulite facies metamorphism. Garnet (30 vol%) is the most abundant mineral phase and appears as irregular subhedral to anhedral porphyroblasts, often exhibiting coronitic microstructure (Fig. 4b). Pyroxene is



Fig. 3 **a** Field occurrence of metavolcanic rocks at the Kribi area. **b** Outcrop view of mafic garnet-biotite gneiss intruded by syenite dyke

Fig. 4 Photographs and microphotographs of the Kribi metavolcanic rocks. Hand specimen of (a) mafic granulite, c garnet-amphibole gneiss, and e garnet-biotite gneiss.

Granoblastic heterogranaular texture (XPL) and mineral composition of (b) mafic granulite, d garnet-amphibole gneiss, and f garnet-biotite gneiss. Mineral abbreviations are after Whitney and Evans (2010). XPL: Crossed-Polarized Light



subhedral to anhedral with a grain size up to 0.5 mm and occurs as clinopyroxene and orthopyroxene (10 vol%) in contact with fine- to coarse-grained quartz and garnet. Plagioclase (15 vol%) occurs as subhedral crystals (1 to 2 mm) and is generally associated with quartz and alkali-feldspar around garnet. Quartz (10 vol%) occurs as subhedral crystals filling spaces between pyroxene. Some quartz grains display wavy and undulose extinctions.

4.1.2 Garnet-amphibole gneiss

Garnet-amphibole gneiss is a fine-grained rock (Fig. 4c), with a granoblastic texture consisting of garnet, amphibole, plagioclase, alkali feldspar, quartz, and biotite (Fig. 4d). Garnet (25 vol%) appears as medium-grained (0.2 to 0.8 mm) and rounded crystals on hand specimen while in thin section, garnet displays anhedral porphyroblasts

commonly associated with plagioclase (15 vol%). Amphibole (15 vol%) occurs as subhedral to anhedral crystals with variable sizes (up to 0.5 mm) in association with subhedral to anhedral alkali feldspar (Fig. 4d). Quartz (15 vol%) shows undulose extinction and is usually associated with alkali feldspar and plagioclase. The latter occurs mainly as anhedral crystals of 1 to 2 mm in size. Alkali-feldspar (10 vol%) occurs as subhedral to anhedral crystals associated with quartz to form the rock matrix. Zircon and rutile form the accessory minerals.

4.1.3 Garnet-biotite gneiss

Garnet-biotite gneiss is the main rock type in the Kribi area and accounts for about 80 % of the exposures. It is a fine-grained light grey rock displaying a gneissose structure (Fig. 4d). In thin section, garnet-biotite gneiss exhibits

granoblastic texture consisting of quartz + alkali feldspar + plagioclase + garnet + biotite (Fig. 4e). The accessory phase includes zircon and magnetite. Quartz is interstitial and usually associated with alkali feldspar and plagioclase. Quartz (30 vol%) is the most abundant mineral of the rock and shows anhedral crystals with variable sizes, up to 0.6 mm. Alkali feldspar (25 vol%) occurs as subhedral to anhedral crystals often exhibiting perthitic microstructure (Fig. 4e). Plagioclase (15 vol%) occurs mainly as anhedral crystals (0.35 mm), though quite a few are developed into stout prismatic grains. Garnet (15 vol%) appears as subhedral to anhedral crystals, some grains contain quartz and biotite inclusions. Biotite (5 vol%) generally appears as fine lamellae (0.1 to 0.2 mm) disseminated within the rock matrix.

4.2 Geochemistry

Seventeen representative samples (7 mafic granulites, 5 garnet-amphibole gneiss, and 5 garnet-biotite gneiss) were analyzed and their whole-rock major and trace element compositions are listed in Tables 1 and 2.

4.2.1 Majors elements

The mafic granulite samples are characterized by low SiO_2 (48.30 to 51.60 wt%) and Al_2O_3 (12.75 to 13.05 wt%) contents compared to garnet-amphibole gneiss (SiO_2 53.80–64.60 wt%; Al_2O_3 15.25–16.20 wt%). Mafic granulites have high MgO (5.21–6.22 wt%), CaO (9.00–10.35 wt%) and Fe_2O_3 (14.4–16.8 wt%) contents, while garnet-amphibole gneiss present lower values (MgO 2.54–3.68 wt%; CaO 4.97–6.88 wt%; Fe_2O_3 6.2–13.45 wt%). In contrast, the garnet-biotite gneiss samples are enriched in SiO_2 (66.10–70.70 wt%) and depleted in CaO (2.25–3.49 wt%) and MgO (0.30–0.60 wt%). Based on the SiO_2 concentrations, the investigated samples comprise two main groups, namely metabasite rocks (mafic granulite and garnet-amphibole gneiss) and metafelsic rocks (garnet-biotite gneiss). All the investigated samples display TiO_2 contents ranging from 0.60 to 1.68 wt%. Their average A/CNK, molar ($\text{Al}_2\text{O}_3/\text{CaO} + \text{Na}_2\text{O} + \text{K}_2\text{O}$), values are 0.57, 0.88 and 0.95, for mafic granulite, garnet-amphibole gneiss and garnet-biotite gneiss, respectively. The mean A/NK, molar ($\text{Al}_2\text{O}_3/\text{Na}_2\text{O} + \text{K}_2\text{O}$), values are slightly high (2.47 for mafic granulite, 2.17 for garnet-amphibole gneiss and 1.55 for garnet-biotite gneiss). The Mg# [$\text{Mg}/[\text{Mg} + 100 \times \text{molar}(\text{MgO}/(\text{MgO} + \text{FeO}))]$] span from 9.18 to 15.49 (garnet-biotite gneiss), from 38.84 to 43.20 (garnet-amphibole gneiss), and from 41.17 to 42.91 (mafic granulite).

4.2.2 Trace and rare earth elements

The Kribi metamorphic rock samples display high field strength element (HFSE) (e.g. Nb, Ta, Zr, and Hf) and large-ion-lithophile elements (LILE) (e.g. Ba, Rb, Cs, K, and Sr) concentrations which increase gradually from metabasite to metafelsic rocks: mafic granulite (Nb = 4.30–5.40; Hf = 1.90–2.60; Ba = 122–146; Rb = 2.20–3), garnet-amphibole gneiss (Nb = 5.50–14; Hf = 3.90–7.40; Ba = 130–841; Rb = 2.20–14.60), garnet-biotite gneiss (Nb = 9.40–15; Hf = 10.70–22, Ba = 2140–3710; Rb = 48.60–96.30). In the NMORB-normalized trace element diagram (Fig. 5a, c, e), the mafic granulite show trace element distribution patterns, with significant enrichment in LILE (Rb, Ba, K) and light-rare-earth-elements (LREE: Nd and Sm) relative to HFSE (Nb, Zr, Ti and Y) and heavy rare-earth-elements (HREE: Dy, Yb and Lu). The multi-element patterns of the garnet-amphibole gneiss show positive anomalies in LILE (Ba and K) and LREE (La and Nd) and negative anomalies in HFSE (Nb, P and Ti). The garnet-biotite gneiss samples show peaks of Rb, Ba, K, and Zr and troughs in Th, Nb, P, and Ti.

The mafic granulite samples have moderate REE contents ($\sum \text{REE} = 53.27$ –84.54 ppm) while the garnet-amphibole gneiss ($\sum \text{REE} = 116.13$ –178.18 ppm) and the garnet-biotite gneiss ($\sum \text{REE} = 243.67$ –332.99 ppm) samples show higher values. On the chondrite-normalized REE diagrams (Fig. 5b, d, f), the mafic granulite samples show relatively flat REE patterns, with slight LREE enrichment ($\text{La}_N/\text{Yb}_N = 1.48$ –2.85; $\text{La}_N/\text{Sm}_N = 1.27$ –2.04; $\text{Gd}_N/\text{Yb}_N = 1.08$ –1.32) and no Eu anomaly ($\text{Eu/Eu}^* = 0.91$ –1.00). The garnet-amphibole gneiss REE patterns are weakly to strongly fractionated ($\text{La}_N/\text{Yb}_N = 3.87$ –15.62), marked by slight LREE ($\text{La}_N/\text{Sm}_N = 2.08$ –4.39) enrichment relative to HREE ($\text{Gd}_N/\text{Yb}_N = 1.40$ –2.15), with significant negative Eu anomalies ($\text{Eu/Eu}^* = 0.56$ –0.82). Garnet-biotite gneiss samples display moderately fractionated REE patterns ($\text{La}_N/\text{Yb}_N = 9.57$ –11.09) with relative enrichment of LREE ($\text{La}_N/\text{Sm}_N = 2.95$ –3.55) over HREE ($\text{Gd}_N/\text{Yb}_N = 1.83$ –2.11) and weak positive Eu anomalies ($\text{Eu/Eu}^* = 1.05$ –1.39). Geochemical data of NE Brazil metavolcanic rocks (Spreatifco et al. 2019) were plotted for comparison. Overall, the trace element distribution patterns of the mafic granulite, garnet-amphibole gneiss, and garnet-biotite gneiss are comparable to those of NE Brazil metabasalt, meta-andesite, and metarhyodacite rocks, respectively (Fig. 5).

4.3 Geochronology

The LA-ICP-MS U-Pb data of the zircon grains from the garnet-biotite gneiss (KR3), are summarized in Table 3. Twenty-eight zircon grains were analysed on which

Table 1 Major elements composition (wt%), molar A/NK, and A/CNK ratios and Mg# of the Kribit metavolcanic rocks

| Rock type | Mafic granulite | | | | | | Garnet-amphibole gneiss | | | | | | Garnet-biotite gneiss | | | | |
|--------------------------------|-----------------|-------|--------|--------|--------|-------|-------------------------|-------|--------|--------|--------|--------|-----------------------|--------|--------|--------|--------|
| | Sample No. | MV1 | MV2 | KR16A | KR16B | KR16C | KR19A | KR19B | KR4A | KR4B | PGKR2 | PGKR4 | KR7A | KR1 | KR2 | KR3 | KR18A |
| SiO ₂ | 51.60 | 51.60 | 50.00 | 48.30 | 50.30 | 51.50 | 51.10 | 56.00 | 53.80 | 64.60 | 64.10 | 62.10 | 70.70 | 69.30 | 67.90 | 69.10 | 66.10 |
| Al ₂ O ₃ | 13.20 | 13.65 | 12.75 | 13.05 | 13.20 | 13.05 | 13.00 | 15.25 | 16.15 | 16.10 | 16.20 | 15.90 | 12.20 | 12.40 | 12.00 | 13.70 | 13.30 |
| Fe ₂ O ₃ | 14.40 | 14.75 | 15.95 | 16.80 | 15.50 | 14.45 | 14.80 | 10.75 | 13.45 | 6.20 | 6.46 | 7.20 | 5.88 | 6.38 | 7.38 | 7.12 | 7.89 |
| CaO | 9.46 | 9.00 | 10.15 | 10.35 | 10.10 | 9.01 | 9.82 | 6.23 | 6.88 | 5.55 | 4.97 | 6.03 | 2.25 | 2.55 | 2.66 | 3.23 | 3.49 |
| MgO | 5.35 | 5.21 | 6.05 | 6.22 | 5.79 | 5.30 | 5.52 | 3.68 | 4.31 | 2.38 | 2.29 | 2.54 | 0.30 | 0.59 | 0.53 | 0.60 | 0.60 |
| Na ₂ O | 2.99 | 2.90 | 2.97 | 2.89 | 3.15 | 3.08 | 3.05 | 3.65 | 3.60 | 4.26 | 4.29 | 4.06 | 2.83 | 2.82 | 2.75 | 2.98 | 2.81 |
| K ₂ O | 0.37 | 0.40 | 0.35 | 0.33 | 0.35 | 0.36 | 0.35 | 0.68 | 0.62 | 0.50 | 1.10 | 1.01 | 3.32 | 3.73 | 3.50 | 3.11 | 2.76 |
| Cr ₂ O ₃ | 0.01 | 0.01 | 0.01 | 0.01 | 0.01 | 0.01 | 0.01 | 0.01 | 0.01 | 0.01 | 0.01 | 0.01 | < 0.01 | < 0.01 | < 0.01 | < 0.01 | < 0.01 |
| TiO ₂ | 1.24 | 1.24 | 1.31 | 1.41 | 1.28 | 1.22 | 1.24 | 1.37 | 1.68 | 0.60 | 0.79 | 0.70 | 0.61 | 0.70 | 0.85 | 0.82 | 0.86 |
| MnO | 0.21 | 0.21 | 0.24 | 0.24 | 0.23 | 0.21 | 0.21 | 0.12 | 0.14 | 0.09 | 0.09 | 0.09 | 0.07 | 0.08 | 0.10 | 0.08 | 0.10 |
| P ₂ O ₅ | 0.11 | 0.09 | 0.14 | 0.10 | 0.17 | 0.13 | 0.18 | 0.27 | 0.32 | 0.20 | 0.22 | 0.22 | 0.18 | 0.21 | 0.25 | 0.29 | 0.32 |
| SrO | 0.03 | 0.03 | 0.01 | 0.01 | 0.01 | 0.01 | 0.02 | 0.05 | 0.05 | 0.05 | 0.06 | 0.05 | 0.04 | 0.04 | 0.04 | 0.05 | 0.05 |
| BaO | 0.02 | 0.03 | 0.01 | 0.01 | 0.01 | 0.01 | 0.01 | 0.01 | 0.04 | 0.05 | 0.04 | 0.09 | 0.07 | 0.33 | 0.31 | 0.30 | 0.26 |
| LOI | 0.42 | 0.45 | 0.68 | 0.41 | 0.48 | 0.45 | 0.54 | 0.51 | 0.44 | 0.43 | 0.46 | 0.54 | 0.37 | 0.51 | 0.43 | 0.30 | 0.27 |
| Total | 99.41 | 99.57 | 100.62 | 100.13 | 100.58 | 98.79 | 99.85 | 98.61 | 101.50 | 101.02 | 101.13 | 100.52 | 99.08 | 99.62 | 98.69 | 101.64 | 98.79 |
| A/CNK | 0.59 | 0.63 | 0.54 | 0.55 | 0.60 | 0.56 | 0.84 | 0.85 | 0.91 | 0.94 | 0.85 | 0.99 | 0.93 | 0.91 | 0.97 | 0.95 | 0.95 |
| A/NK | 2.48 | 2.62 | 2.42 | 2.55 | 2.38 | 2.39 | 2.41 | 2.26 | 2.45 | 2.13 | 1.97 | 2.05 | 1.48 | 1.43 | 1.44 | 1.66 | 1.75 |
| Mg# | 42.40 | 41.17 | 42.91 | 42.32 | 42.54 | 42.09 | 40.42 | 38.84 | 43.20 | 41.26 | 41.14 | 9.18 | 15.49 | 12.46 | 14.31 | 13.10 | |

Table 2 Trace and REE elements contents (ppm) and elemental ratios of the Kribi metavolcanic rocks

| Rock type | Mafic granulite | | | | | | Garnet-amphibole gneiss | | | | | | Garnet-biotite gneiss | | | | |
|-----------|-----------------|--------|--------|--------|--------|--------|-------------------------|--------|--------|---------|--------|---------|-----------------------|---------|---------|---------|---------|
| | Sample No. | MV1 | MV2 | KR16A | KR16B | KR16C | KR19A | KR19B | KR4A | KR4B | PGKR2 | PGKR4 | KR7A | KR1 | KR2 | KR3 | KR18A |
| Ba | 228.00 | 246.00 | 126.00 | 129.50 | 122.00 | 129.00 | 130.00 | 417.00 | 432.00 | 383.00 | 841.00 | 661.00 | 3710.00 | 3020.00 | 2930.00 | 2360.00 | 2140.00 |
| Rb | 3.00 | 2.80 | 2.70 | 2.20 | 2.20 | 2.40 | 2.50 | 5.80 | 6.00 | 2.20 | 14.60 | 5.50 | 96.30 | 73.80 | 67.70 | 56.60 | 48.60 |
| Sr | 222.00 | 237.00 | 95.40 | 97.80 | 99.10 | 122.00 | 123.00 | 428.00 | 431.00 | 453.00 | 449.00 | 400.00 | 358.00 | 310.00 | 279.00 | 382.00 | 362.00 |
| Zr | 87.00 | 60.00 | 57.00 | 73.00 | 53.00 | 68.00 | 55.00 | 189.00 | 224.00 | 183.00 | 229.00 | 280.00 | 810.00 | 708.00 | 1050.00 | 410.00 | 525.00 |
| Nb | 5.40 | 4.70 | 4.90 | 5.00 | 4.50 | 4.30 | 4.50 | 11.70 | 14.00 | 5.50 | 11.60 | 6.00 | 13.70 | 9.40 | 15.00 | 14.30 | 13.90 |
| Ta | 0.60 | 0.50 | 0.60 | 0.50 | 0.70 | 0.30 | 0.40 | 0.50 | 0.50 | 0.30 | 0.40 | 0.10 | 0.70 | 0.50 | 0.70 | 0.60 | 0.60 |
| U | 0.28 | 0.26 | 0.20 | 0.26 | 0.22 | 0.18 | 0.19 | 0.25 | 0.22 | 0.11 | 0.19 | 0.10 | 1.14 | 0.52 | 0.46 | 0.28 | 0.35 |
| Cr | 70.00 | 60.00 | 60.00 | 60.00 | 60.00 | 50.00 | 50.00 | 60.00 | 60.00 | 50.00 | 50.00 | 40.00 | 20.00 | 20.00 | 20.00 | 20.00 | 10.00 |
| Ga | 22.00 | 20.50 | 20.00 | 22.10 | 20.40 | 19.10 | 19.40 | 23.70 | 23.80 | 20.70 | 20.20 | 21.70 | 23.90 | 20.10 | 21.00 | 22.50 | 23.10 |
| Hf | 2.60 | 1.90 | 2.20 | 2.60 | 1.90 | 2.40 | 2.20 | 5.40 | 6.00 | 3.90 | 5.10 | 7.40 | 16.50 | 15.40 | 22.00 | 10.70 | 13.40 |
| V | 379.00 | 371.00 | 409.00 | 430.00 | 383.00 | 359.00 | 378.00 | 234.00 | 291.00 | 104.00 | 104.00 | 129.00 | 15.00 | 31.00 | 29.00 | 32.00 | 30.00 |
| Y | 27.70 | 24.10 | 31.30 | 29.50 | 29.30 | 23.10 | 26.10 | 43.50 | 52.60 | 19.00 | 18.30 | 31.40 | 35.50 | 32.90 | 45.90 | 33.80 | 38.40 |
| Zr/Hf | 3.14 | 2.49 | 1.82 | 2.47 | 1.81 | 2.94 | 2.11 | 4.34 | 4.26 | 9.63 | 12.51 | 8.92 | 22.82 | 21.52 | 22.88 | 12.13 | 13.67 |
| Ta/Yb | 0.23 | 0.20 | 0.19 | 0.16 | 0.24 | 0.13 | 0.16 | 0.12 | 0.10 | 0.17 | 0.24 | 0.04 | 0.20 | 0.16 | 0.15 | 0.19 | 0.17 |
| Th/Yb | 0.18 | 0.18 | 0.20 | 0.23 | 0.20 | 0.21 | 0.25 | 0.19 | 0.15 | 0.08 | 0.63 | 0.06 | 0.65 | 0.76 | 0.51 | 0.16 | 0.17 |
| Ta/Hf | 0.23 | 0.26 | 0.27 | 0.19 | 0.37 | 0.13 | 0.18 | 0.09 | 0.08 | 0.08 | 0.08 | 0.01 | 0.04 | 0.03 | 0.03 | 0.06 | 0.04 |
| Th/Hf | 0.18 | 0.23 | 0.30 | 0.27 | 0.31 | 0.20 | 0.29 | 0.15 | 0.12 | 0.04 | 0.21 | 0.02 | 0.14 | 0.16 | 0.11 | 0.05 | 0.04 |
| Th/Nb | 0.09 | 0.09 | 0.13 | 0.14 | 0.13 | 0.11 | 0.14 | 0.07 | 0.05 | 0.03 | 0.09 | 0.03 | 0.16 | 0.26 | 0.16 | 0.03 | 0.04 |
| La/Nb | 2.00 | 2.19 | 1.51 | 1.36 | 1.71 | 1.58 | 1.84 | 2.34 | 2.03 | 3.76 | 3.34 | 4.42 | 3.50 | 5.51 | 4.37 | 3.49 | 3.88 |
| Nb/Th | 11.49 | 10.93 | 7.54 | 7.04 | 7.76 | 8.78 | 7.03 | 14.81 | 19.18 | 36.67 | 10.94 | 35.29 | 6.12 | 3.87 | 6.28 | 29.18 | 23.17 |
| Nb/Yb | 2.09 | 1.93 | 1.52 | 1.60 | 1.56 | 1.88 | 1.77 | 2.76 | 2.80 | 3.06 | 6.86 | 2.25 | 3.98 | 2.96 | 3.22 | 4.53 | 3.84 |
| Th/Yb | 0.18 | 0.18 | 0.20 | 0.23 | 0.20 | 0.21 | 0.25 | 0.19 | 0.15 | 0.08 | 0.63 | 0.06 | 0.65 | 0.76 | 0.51 | 0.16 | 0.17 |
| Th/La | 0.04 | 0.04 | 0.09 | 0.10 | 0.08 | 0.07 | 0.08 | 0.03 | 0.03 | 0.01 | 0.03 | 0.01 | 0.05 | 0.05 | 0.04 | 0.01 | 0.01 |
| Nb/Ta | 9.00 | 9.40 | 8.17 | 10.00 | 6.43 | 14.33 | 11.25 | 23.40 | 28.00 | 18.33 | 29.00 | 60.00 | 19.57 | 18.80 | 21.43 | 23.83 | 23.17 |
| Lu/Yb | 0.16 | 0.16 | 0.15 | 0.15 | 0.16 | 0.15 | 0.16 | 0.14 | 0.14 | 0.15 | 0.15 | 0.15 | 0.18 | 0.14 | 0.16 | 0.15 | 0.15 |
| Nb/La | 0.50 | 0.46 | 0.66 | 0.74 | 0.58 | 0.63 | 0.54 | 0.43 | 0.49 | 0.27 | 0.30 | 0.23 | 0.29 | 0.18 | 0.23 | 0.29 | 0.26 |
| Nb/Y | 0.19 | 0.20 | 0.16 | 0.17 | 0.15 | 0.19 | 0.17 | 0.27 | 0.27 | 0.29 | 0.63 | 0.19 | 0.39 | 0.29 | 0.33 | 0.42 | 0.36 |
| La/Yb | 4.19 | 4.22 | 2.30 | 2.17 | 2.67 | 2.97 | 3.27 | 6.46 | 5.68 | 11.50 | 22.96 | 9.93 | 13.95 | 16.29 | 14.06 | 15.79 | 14.89 |
| Dy/Yb | 1.74 | 1.70 | 1.55 | 1.50 | 1.63 | 1.75 | 1.79 | 1.96 | 2.02 | 1.87 | 2.01 | 2.36 | 2.01 | 2.02 | 1.82 | 2.06 | 2.09 |
| La/Sm | 2.90 | 3.25 | 2.03 | 2.09 | 2.24 | 2.31 | 2.46 | 3.76 | 3.31 | 4.25 | 7.00 | 3.66 | 4.71 | 5.03 | 5.16 | 5.67 | 5.46 |
| U/Th | 0.60 | 0.60 | 0.31 | 0.37 | 0.38 | 0.37 | 0.30 | 0.32 | 0.30 | 0.73 | 0.18 | 0.59 | 0.51 | 0.21 | 0.19 | 0.57 | 0.58 |
| Ba/Th | 485.11 | 572.09 | 193.85 | 182.39 | 210.34 | 263.27 | 203.13 | 527.85 | 591.78 | 2533.33 | 793.40 | 3888.24 | 1656.25 | 1242.80 | 1225.94 | 4816.33 | 3566.67 |
| La | 10.80 | 10.30 | 7.40 | 6.80 | 7.70 | 6.80 | 8.30 | 27.40 | 28.40 | 20.70 | 38.80 | 26.50 | 48.00 | 51.80 | 65.50 | 49.90 | 53.90 |
| Ce | 22.70 | 21.00 | 17.30 | 15.80 | 17.70 | 15.60 | 19.40 | 58.00 | 61.70 | 45.80 | 75.80 | 60.00 | 96.80 | 105.00 | 135.00 | 98.70 | 107.50 |

Table 2 continued

| Rock type | Mafic granulite | | | | | | Garnet-amphibole gneiss | | | | | | Garnet-biotite gneiss | | | | |
|----------------------|-----------------|-------|-------|-------|-------|-------|-------------------------|--------|--------|--------|--------|--------|-----------------------|--------|--------|--------|--------|
| | Sample No. | MV1 | MV2 | KR16A | KR16B | KR16C | KR19A | KR19B | KR4A | KR4B | PGKR2 | PGKR4 | KR7A | KR1 | KR2 | KR3 | KR18A |
| Pr | 3.07 | 2.67 | 2.38 | 2.25 | 2.42 | 2.19 | 2.63 | 7.34 | 7.86 | 5.83 | 8.73 | 7.90 | 12.05 | 12.70 | 16.20 | 11.65 | 12.70 |
| Nd | 13.70 | 11.80 | 11.20 | 10.60 | 11.20 | 10.10 | 12.40 | 31.40 | 34.60 | 24.70 | 33.30 | 33.80 | 51.90 | 52.50 | 66.40 | 46.70 | 51.10 |
| Sm | 3.73 | 3.17 | 3.64 | 3.25 | 3.44 | 2.95 | 3.37 | 7.29 | 8.57 | 5.54 | 7.25 | 10.20 | 10.30 | 12.70 | 8.80 | 9.87 | |
| Eu | 1.20 | 1.12 | 1.16 | 1.12 | 1.08 | 1.12 | 1.82 | 1.95 | 1.21 | 1.33 | 1.31 | 4.24 | 3.60 | 3.96 | 2.94 | 3.30 | |
| Gd | 4.10 | 3.96 | 4.11 | 4.16 | 4.10 | 3.69 | 4.25 | 7.34 | 9.34 | 4.12 | 4.42 | 7.07 | 8.53 | 7.79 | 10.50 | 8.22 | 9.15 |
| Tb | 0.67 | 0.66 | 0.72 | 0.70 | 0.71 | 0.62 | 0.72 | 1.25 | 1.51 | 0.59 | 0.56 | 1.05 | 1.18 | 1.08 | 1.49 | 1.14 | 1.28 |
| Dy | 4.49 | 4.15 | 4.99 | 4.71 | 4.69 | 4.00 | 4.55 | 8.29 | 10.10 | 3.37 | 3.40 | 6.31 | 6.92 | 6.43 | 8.46 | 6.52 | 7.58 |
| Ho | 0.97 | 0.90 | 1.06 | 1.05 | 0.99 | 0.86 | 0.99 | 1.73 | 2.03 | 0.71 | 0.65 | 1.24 | 1.37 | 1.27 | 1.75 | 1.37 | 1.51 |
| Er | 2.90 | 2.62 | 3.05 | 3.27 | 2.89 | 2.40 | 2.78 | 4.72 | 5.60 | 1.88 | 2.02 | 3.05 | 3.83 | 3.56 | 4.84 | 3.60 | 4.11 |
| Tm | 0.39 | 0.36 | 0.50 | 0.46 | 0.44 | 0.35 | 0.41 | 0.66 | 0.83 | 0.28 | 0.30 | 0.46 | 0.54 | 0.54 | 0.79 | 0.50 | 0.58 |
| Yb | 2.58 | 2.44 | 3.22 | 3.13 | 2.88 | 2.29 | 2.54 | 4.24 | 5.00 | 1.80 | 1.69 | 2.67 | 3.44 | 3.18 | 4.66 | 3.16 | 3.62 |
| Lu | 0.40 | 0.39 | 0.48 | 0.48 | 0.46 | 0.34 | 0.40 | 0.58 | 0.69 | 0.27 | 0.26 | 0.40 | 0.61 | 0.45 | 0.74 | 0.47 | 0.55 |
| Sum_REE | 71.70 | 65.54 | 61.21 | 57.78 | 60.74 | 53.27 | 63.86 | 162.06 | 178.18 | 116.13 | 176.80 | 159.01 | 249.61 | 260.20 | 332.99 | 243.67 | 266.75 |
| (La/Yb) _N | 2.85 | 2.87 | 1.56 | 1.48 | 1.82 | 2.02 | 2.22 | 4.40 | 3.87 | 7.83 | 15.62 | 6.75 | 9.50 | 11.09 | 9.57 | 10.75 | 10.13 |
| (Ce/Sm) _N | 1.48 | 1.61 | 1.15 | 1.18 | 1.25 | 1.28 | 1.40 | 1.93 | 1.75 | 2.28 | 3.32 | 2.01 | 2.30 | 2.47 | 2.58 | 2.72 | 2.64 |
| (Gd/Yb) _N | 1.29 | 1.32 | 1.04 | 1.08 | 1.15 | 1.31 | 1.36 | 1.40 | 1.51 | 1.86 | 2.12 | 2.15 | 2.01 | 1.99 | 1.83 | 2.11 | 2.05 |
| Ce/Ce* | 0.95 | 0.97 | 1.00 | 0.98 | 0.99 | 0.98 | 1.01 | 0.99 | 1.00 | 1.01 | 1.00 | 1.00 | 0.97 | 0.99 | 1.00 | 0.99 | 1.00 |
| Eu/Eu* | 0.94 | 0.96 | 0.92 | 0.93 | 0.91 | 1.00 | 0.90 | 0.76 | 0.67 | 0.82 | 0.82 | 0.56 | 1.39 | 1.23 | 1.05 | 1.05 | 1.06 |

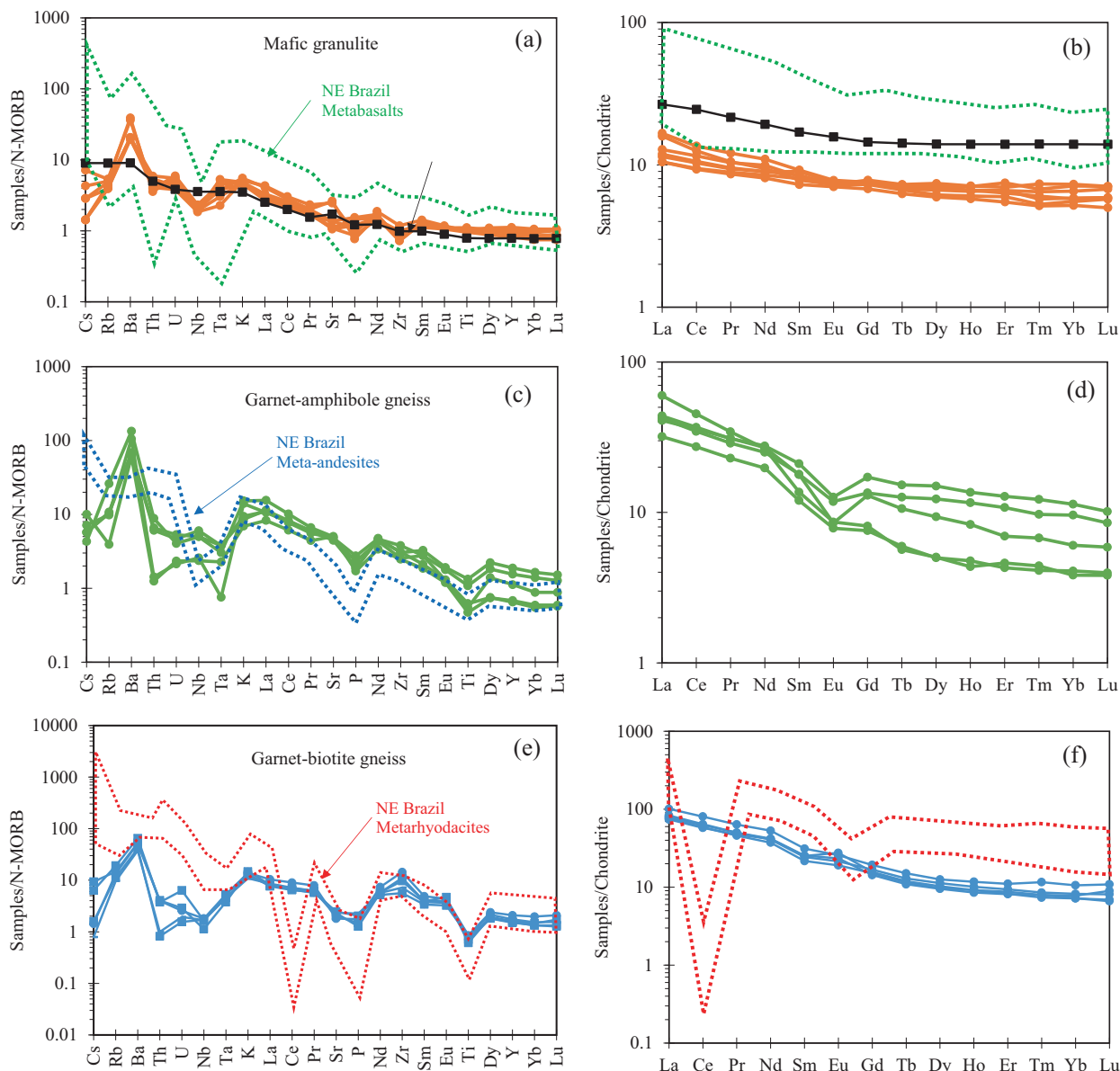


Fig. 5 NMORB normalized trace element concentration patterns (a, c, e), and Chondrite-normalized REE patterns (b, d, f) of the Kribi metavolcanic rocks. The primitive mantle- and chondrite-normalized values are from Sun and McDonough (1989). Geochemical data of NE Brazil metavolcanic rocks (Spreafico et al. 2019) are plotted for comparison

twenty-seven reliable U-Pb age analytical spots with 95–102 % concordance were obtained. Investigated zircon grains were 50–200 μm long with crack-free crystal faces. Euhedral zircons are rare as most grains are subhedral to anhedral in shape. Very few zircons show simple evolved prism shapes, but most crystals have either rounded or multi-faceted shapes. The rounded grains usually exhibit multiple crystal faces, similar to the so-called ‘soccerball zircons’ (Schaltegger et al. 1999). On Cathodoluminescence (CL) imaging, most zircon grains exhibit complex internal structures, dominated by featureless domains and planar growth banding (Fig. 6a). Oscillatory growth zonation is

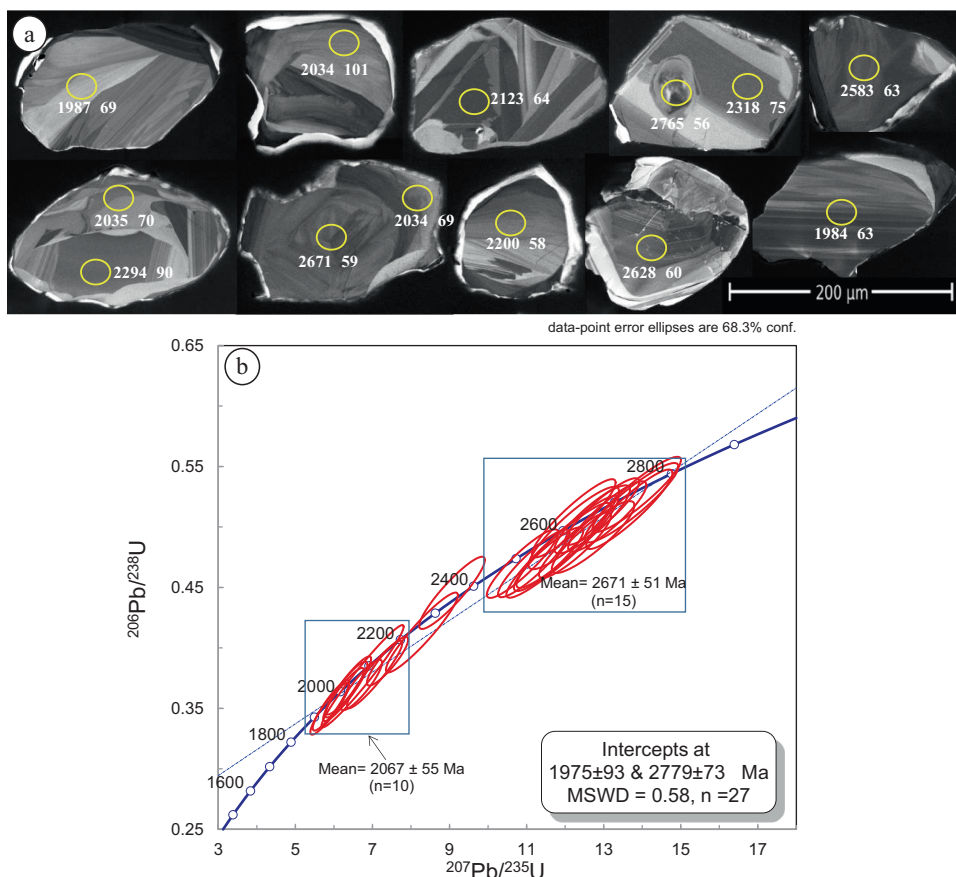
mainly absent. A few grains display low-CL domains surrounding a high-CL central part, which could be interpreted as a relict core with significant overgrowth. Zircon recrystallization is also evidenced by homogeneous crystal domains and distinct reaction fronts.

All analyzed spots have high Th/U ratios (0.13–0.72; >0.1), suggesting that these zircons have a magmatic origin (Belousova et al. 2002; Wu and Zheng 2004), but their internal structures suggest that they have been recrystallized by metamorphic processes. On the U-Pb Concordia diagram, the analyzed data indicate an upper intercept age

Table 3 LA-ICP-MS U-Pb analytical data of zircon from the Kribi metaryhodacite

| Spots | Th/U | Isotopic ratios | | | | | | Apparent ages | | | | | | | |
|--------|------|-----------------------------------|------|----------------------------------|-------|----------------------------------|------|---------------|-----------------------------------|--------|----------------------------------|-------|----------------------------------|--------|-----------|
| | | $^{207}\text{Pb}/^{206}\text{Pb}$ | 1s | $^{207}\text{Pb}/^{235}\text{U}$ | 1s | $^{206}\text{Pb}/^{238}\text{U}$ | 1s | Rho | $^{207}\text{Pb}/^{206}\text{Pb}$ | 1s | $^{207}\text{Pb}/^{235}\text{U}$ | 1s | $^{206}\text{Pb}/^{238}\text{U}$ | 1s | conc. (%) |
| KR3-01 | 0.14 | 0.08 | 3.48 | 3.10 | 5.02 | 0.27 | 3.62 | 0.90 | 1295.10 | 67.65 | 1432.27 | 38.52 | 1526.37 | 49.16 | 117.86 |
| KR3-02 | 0.41 | 0.18 | 3.54 | 12.70 | 5.10 | 0.51 | 3.67 | 0.88 | 2671.32 | 58.55 | 2657.99 | 47.98 | 2640.52 | 79.54 | 98.85 |
| KR3-03 | 0.66 | 0.13 | 3.87 | 6.25 | 5.57 | 0.36 | 4.01 | 0.91 | 2034.02 | 68.52 | 2011.25 | 48.79 | 1989.15 | 68.62 | 97.79 |
| KR3-04 | 0.46 | 0.13 | 7.35 | 6.74 | 10.44 | 0.38 | 7.41 | 0.97 | 2096.19 | 129.18 | 2078.43 | 92.32 | 2060.56 | 130.73 | 98.30 |
| KR3-05 | 0.53 | 0.19 | 3.89 | 12.73 | 5.57 | 0.49 | 3.99 | 0.89 | 2722.72 | 64.02 | 2659.74 | 52.41 | 2577.71 | 84.70 | 94.67 |
| KR3-06 | 0.35 | 0.12 | 3.55 | 5.92 | 5.28 | 0.35 | 3.91 | 0.91 | 1983.88 | 63.14 | 1964.75 | 45.84 | 1946.64 | 65.62 | 98.12 |
| KR3-07 | 0.72 | 0.13 | 5.71 | 5.90 | 8.16 | 0.34 | 5.82 | 0.94 | 2033.96 | 101.09 | 1960.66 | 70.81 | 1891.99 | 95.46 | 93.02 |
| KR3-08 | 0.50 | 0.19 | 3.47 | 13.10 | 5.12 | 0.51 | 3.77 | 0.89 | 2713.40 | 57.14 | 2686.53 | 48.32 | 2650.96 | 81.98 | 97.70 |
| KR3-09 | 0.50 | 0.19 | 3.39 | 13.67 | 5.41 | 0.51 | 4.22 | 0.92 | 2764.79 | 55.71 | 2727.03 | 51.21 | 2676.34 | 92.34 | 96.80 |
| KR3-10 | 0.41 | 0.14 | 8.30 | 7.06 | 6.71 | 0.38 | 4.87 | 0.93 | 2168.94 | 137.91 | 2118.56 | 58.02 | 2067.05 | 85.71 | 95.30 |
| KR3-11 | 0.44 | 0.18 | 5.62 | 11.93 | 8.04 | 0.48 | 5.75 | 0.94 | 2642.57 | 93.28 | 2598.81 | 75.31 | 2543.04 | 120.80 | 96.23 |
| KR3-12 | 0.45 | 0.17 | 3.95 | 10.89 | 5.61 | 0.47 | 3.98 | 0.90 | 2540.14 | 66.23 | 2514.20 | 52.16 | 2482.19 | 82.03 | 97.72 |
| KR3-13 | 0.44 | 0.18 | 4.76 | 11.96 | 6.75 | 0.48 | 4.79 | 0.93 | 2643.25 | 79.08 | 2601.43 | 63.28 | 2548.07 | 100.73 | 96.40 |
| KR3-14 | 0.49 | 0.19 | 4.12 | 13.72 | 5.86 | 0.52 | 4.17 | 0.91 | 2754.11 | 67.73 | 2730.80 | 55.47 | 2699.39 | 91.86 | 98.01 |
| KR3-15 | 0.46 | 0.13 | 3.68 | 6.71 | 5.24 | 0.37 | 3.74 | 0.88 | 2122.56 | 64.45 | 2074.57 | 46.35 | 2026.58 | 64.99 | 95.48 |
| KR3-16 | 0.45 | 0.14 | 3.33 | 7.39 | 4.77 | 0.39 | 3.42 | 0.88 | 2199.75 | 57.89 | 2159.91 | 42.69 | 2118.24 | 61.68 | 96.29 |
| KR3-17 | 0.44 | 0.18 | 4.46 | 12.23 | 6.34 | 0.50 | 4.51 | 0.90 | 2630.96 | 74.09 | 2621.85 | 59.51 | 2610.06 | 96.75 | 99.21 |
| KR3-18 | 0.41 | 0.12 | 3.89 | 5.89 | 5.60 | 0.35 | 4.03 | 0.91 | 1987.38 | 69.13 | 1959.35 | 48.60 | 1932.92 | 67.32 | 97.26 |
| KR3-19 | 0.51 | 0.18 | 3.40 | 12.96 | 4.91 | 0.51 | 3.54 | 0.90 | 2683.23 | 56.17 | 2676.79 | 46.28 | 2668.28 | 77.45 | 99.44 |
| KR3-20 | 0.45 | 0.13 | 4.24 | 6.38 | 6.03 | 0.37 | 4.29 | 0.92 | 2035.19 | 74.97 | 2029.85 | 52.93 | 2024.60 | 74.54 | 99.48 |
| KR3-21 | 0.43 | 0.19 | 3.85 | 13.86 | 5.47 | 0.53 | 3.89 | 0.92 | 2748.88 | 63.20 | 2740.17 | 51.82 | 2728.37 | 86.58 | 99.25 |
| KR3-22 | 0.46 | 0.18 | 3.61 | 11.57 | 5.14 | 0.47 | 3.66 | 0.90 | 2627.82 | 59.99 | 2570.42 | 48.06 | 2498.27 | 75.88 | 95.07 |
| KR3-23 | 0.46 | 0.18 | 3.42 | 12.26 | 5.04 | 0.48 | 3.69 | 0.90 | 2682.99 | 56.63 | 2624.28 | 47.27 | 2548.86 | 77.72 | 95.00 |
| KR3-24 | 0.41 | 0.17 | 4.09 | 12.23 | 5.86 | 0.51 | 4.20 | 0.92 | 2604.54 | 68.08 | 2621.96 | 55.02 | 2644.57 | 91.18 | 101.54 |
| KR3-25 | 0.50 | 0.13 | 3.97 | 6.32 | 5.75 | 0.37 | 4.16 | 0.89 | 2034.82 | 70.27 | 2021.46 | 50.39 | 2008.41 | 71.70 | 98.70 |
| KR3-26 | 0.46 | 0.17 | 3.79 | 11.19 | 5.47 | 0.47 | 3.93 | 0.91 | 2583.41 | 63.35 | 2538.77 | 50.95 | 2483.30 | 81.09 | 96.12 |
| KR3-27 | 0.48 | 0.15 | 4.36 | 9.07 | 6.21 | 0.45 | 4.42 | 0.91 | 2318.15 | 74.82 | 2344.68 | 56.82 | 2375.28 | 87.88 | 102.46 |
| KR3-28 | 0.43 | 0.15 | 5.25 | 8.28 | 7.45 | 0.41 | 5.28 | 0.94 | 2294.32 | 90.31 | 2262.52 | 67.45 | 2227.51 | 99.38 | 97.09 |

Fig. 6 **a** Representative zircon CL images. Yellow circles represent spots used for U-Pb dating. **b** Concordia plot with pooled results representing intercepts and weighted mean $^{206}\text{Pb}/^{207}\text{Pb}$ ages of the garnet-biotite gneiss (sample KR3)



of $2779 \pm 73 \text{ Ma}$, and a lower intercept age of $1975 \pm 95 \text{ Ma}$ ($\text{MSWD} = 0.53$) (Fig. 6b). Then concordant spots yield weighed mean Pb-Pb of $2067 \pm 55 \text{ Ma}$ (95 % conf.) for the young cluster, and fifteen concordant spots a weighted mean Pb-Pb of $2671 \pm 51 \text{ Ma}$ (96.5 % conf.) for the old cluster.

5 Discussion

5.1 Protolith reconstruction

The mafic granulite and garnet-amphibole gneiss samples with SiO_2 contents of 48.30 to 64.6 wt% and moderate Mg# (mean: 42.28 and 40.97, respectively) will be referred to as metabasite rocks, while garnet-biotite gneiss samples are metafelsic rocks due to their silica enrichment ($\text{SiO}_2 > 66 \text{ wt\%}$) and low Mg# (mean: 12.91).

To constrain the nature of the protolith of the Kribi metamorphic rocks, MnO versus TiO_2 (Garrels and Mackenzie 1971) diagram was used and all samples plot in the igneous protolith field (Fig. 7a and b). On the Zr/TiO_2 vs. Nb/Y (Winchester and Floyd 1977) discrimination diagram (Fig. 7c), mafic granulite samples plot into the basalt field whereas garnet-amphibole gneiss samples fall

in basaltic andesite field. NE Brazil metabasalts (Spreafico et al. 2019) and the Nyong Group metabasite rocks (Loose and Schenk 2018; Moudiob et al. 2020; Kwamou et al. 2021) were plotted for comparison and showed similar chemistry. All the studied samples pertain to the meta-aluminous rocks due to their low A/CNK values < 1 and belong to the tholeiitic (mafic granulite), transitional to calc-alkaline (garnet-amphibole gneiss), and calc-alkaline (garnet-biotite gneiss) series (Fig. 7d).

5.2 Element mobility assessment

The Kribi area metavolcanic rocks have been affected by post-igneous processes such as deformation, metamorphism, and alteration, which could have obliterated their primary features (Polat et al. 2000). Therefore, it is important to evaluate the element mobility before any petrogenetic interpretation. Petrological characteristics show that the investigated samples experienced retrograde granulite facies metamorphism and thin sections observations exhibited mineral transformations such as pyroxene into amphibole or amphibole into biotite. Geochemical analyses show that all the samples have low loss on ignition (LOI) values ($< 1 \%$) suggesting that they have not been strongly altered, hydrated or carbonated. The absence

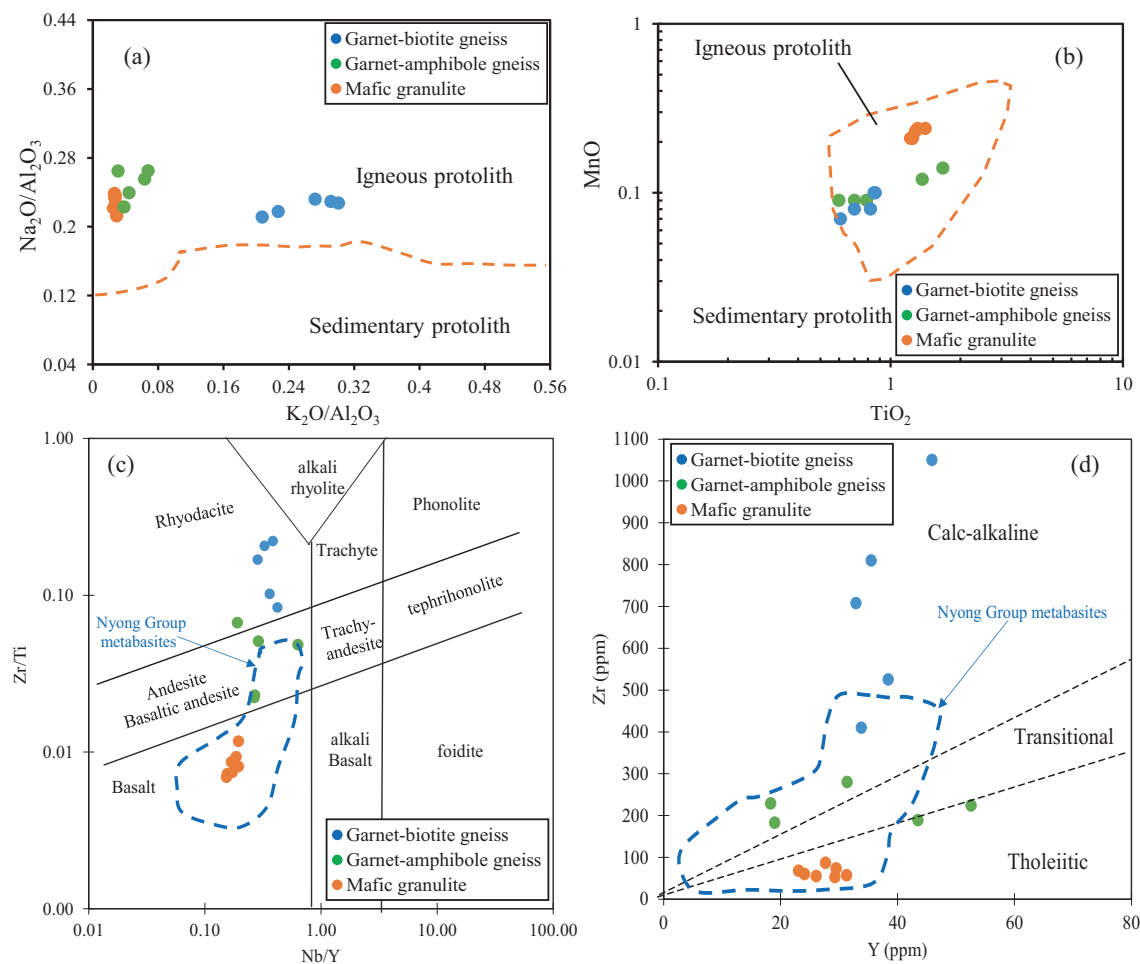


Fig. 7 Geochemical classification diagrams for the studied rocks. **a** and **b** Na_2O vs. Al_2O_3 (Werner 1987) and MnO vs. TiO_2 (Garrels and Mackenzie 1971) protolith reconstruction diagrams. **c** Plot of Zr/Ti vs. Nb/Y (Winchester and Floyd 1977). **d** Plot of Zr vs. Yb (MacLean and Barrett 1993). The boundary line between tholeiitic and calc-alkaline rock types is from Miyashiro (1974)

of Ce anomalies ($0.9 < \text{Ce/Ce}^* < 1.1$) in the studied metavolcanic rocks indicates limited REE mobility (Polat et al. 2002). They show coherent patterns in the chondrite-normalized REE and NMORB-normalized trace element diagrams (Fig. 5), suggesting that these elements were largely preserved during subsequent alteration and metamorphism, and thus can be used to assess the characteristics of their protoliths (Taylor et al. 1986; Middelburg et al. 1988). In addition, LIL (Ba and Nd) and HFS (Nb and Hf) elements are plotted against Zr (Polat et al. 2002; Fig. 8), because Zr in igneous rocks is generally considered the most immobile during metamorphism and alteration, except for the case of seafloor-hydrothermal alteration (Wood et al. 1979; Gibson et al. 1983). Although Ba and Nb show a weak correlation, suggesting some degree of mobility of these elements, Hf, Nd, Sm, and ΣREE (Fig. 8c-f) correlate well with Zr for the majority of the investigated samples, which confirm the use of immobile trace elements for protolith identification. The

aforementioned indicates that the most immobile trace element compositions of the studied rocks could be used for petrogenetic purposes.

5.3 Crustal contamination

Generally, primary magma reflects the conditions of partial melting and the composition of the source area where they derived (Klein and Langmuir 1987; Niu et al. 2002; Zhang et al. 2006; Niu and O'Hara 2008). However, the primary magma composition can be modified by variable crustal contamination or shallow level processes (e.g. fractional crystallization) during the magma intrusion and cooling process. The mafic granulite samples show lower SiO_2 (mean: 50.53), MgO (mean: 5.63), and higher Fe_2O_3 (mean: 15.24) contents than the garnet-amphibole gneiss (mean SiO_2 : 60.2, MgO : 3.04; Fe_2O_3 : 8.81), which might be due to crustal contamination during the emplacement of the garnet-amphibole gneiss protoliths. According to

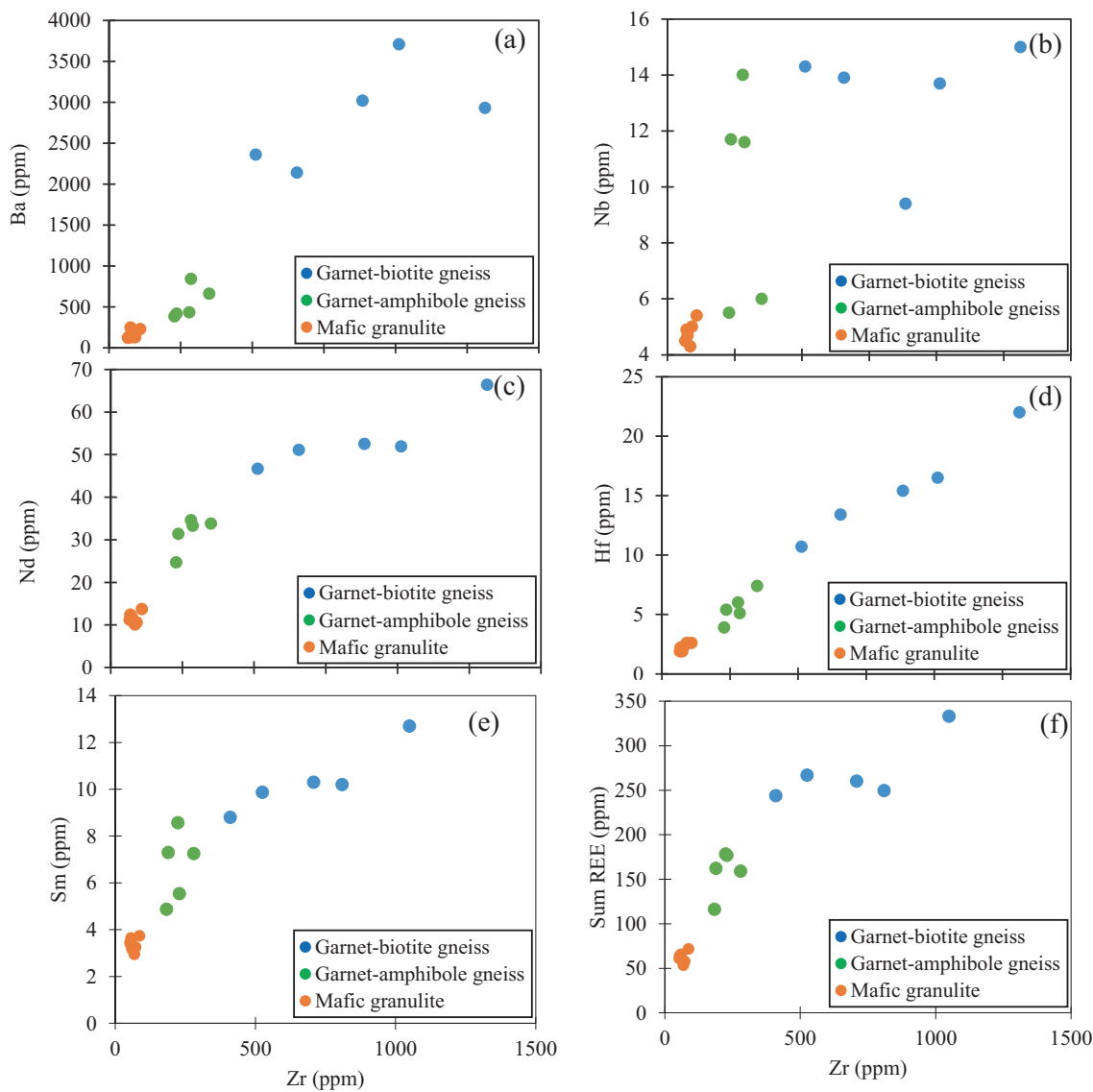


Fig. 8 Binary plots of selected trace elements against Zr

Taylor and McLennan (1985), positive Zr anomalies, high Th/Nb ratios, and LREE-enrichment are features of crustal contaminated mafic rocks. The low Th/Nb ratios in mafic granulite (mean: 0.12) to very low (mean: 0.05) in garnet-amphibole gneiss, LREE enrichment patterns in garnet-amphibole gneiss, and slightly in mafic granulite, and the small negative Zr anomaly of the studied metabasite rocks suggest that these rocks were slightly affected by crustal contamination. Furthermore, their average Nb/Ta, Lu/Yb, Nb/La, and Rb/La ratios which are 9.80 and 31.75; 0.15 and 0.15, 0.59 and 0.34; 0.31 and 0.22 for mafic granulite and garnet-amphibole gneiss respectively indicate the influence of variable degrees of crustal components (Taylor and McLennan 1985; Sun and McDonough 1989; Pearce and Peate 1995; Condie 2005; Pearce 2008; Zhou et al. 2009; Dai et al. 2011). Therefore, it is suggested that the

studied metabasite rock samples have suffered some degree of crustal contamination.

5.4 Petrogenesis

5.4.1 Genesis of metabasite rocks

The Mg# values (39–43) of the Kribi metabasite rocks are less than those of primary magma (68–75, Wilson 1989), indicating that they could derive from the crystal fractionation of mafic minerals during magma genesis. Low MgO combined to moderate to high Fe₂O₃ contents suggest fractional crystallization of Mg-rich minerals (i.e., olivine, orthopyroxene) which is typical of tholeiitic magmas (Irvine and Baragar 2011). On the Fenner diagrams (Fig. 9a, b, and c), MgO show positive correlations with

$\text{CaO}/\text{Al}_2\text{O}_3$, Fe_2O_3 , and TiO_2 . The $\text{CaO}/\text{Al}_2\text{O}_3$ decrease with decreasing MgO suggesting the precipitation of clinopyroxene and/or plagioclase (Fig. 9a). The depletion of MgO with decreasing Fe_2O_3 and TiO_2 abundances (Fig. 9b, c) is the result of Fe-Ti oxide fractionation, consistent with accessory minerals (e.g., magnetite and titanite). Negative anomalies of Ti in multielement diagrams could also indicate fractionation of Ti-enriched oxides. The studied metabasite rocks are marked by a lack of Ti anomaly in the mafic granulite samples while the garnet-amphibole gneiss shows a negative Ti anomaly supporting Ti oxide fractionation (Fig. 5a, c). Plagioclase fractionation in mafic granulite samples did not play a role in the source of their protolith as they show a lack of Eu anomalies (Eu/Eu^* : 0.9–1) on chondrite normalized REE diagrams. Conversely, biotite-amphibole gneiss show negative Eu anomalies (Eu/Eu^* : 0.56–0.82) and troughs in Sr in multielement diagrams indicating plagioclase fractionation (Fig. 5d). Similarly, mafic granulite samples in contrast to garnet-amphibole gneiss show relatively flat REE patterns, suggesting that only slight fractional

crystallisation may have operated during igneous differentiation (Wilson 1989). On La/Sm vs. La diagram (Blein et al. 2001; Fig. 9d), mafic granulite samples present a positive trend, suggesting that partial melting could be the main process that operated during the igneous differentiation. The garnet-amphibole gneiss samples show relatively scattered data indicating that both partial melting and fractional crystallization processes may have operated. Therefore it is suggested that the garnet-amphibole gneiss protolith was derived from the crystal fractionation of basaltic magma. In addition, the negligible changes in the Nb/La and Nb/Ce ratios among the metabasite rock samples also fully support the derivation of the basaltic andesite from basalts. Many authors (e.g. Pearce and Cann 1973; Jung et al. 2006; Zhang et al. 2006, 2012a, b; Geng et al. 2011; Xia et al. 2018) proposed the use of immobile elements (e.g. incompatible trace elements and REE) to constrain the magma source. Multielement and chondrite normalized REE patterns of the mafic granulite are comparable to those of E-MORB produced from a depleted mantle source (Fig. 5a and b). On the Nb vs. Zr diagram

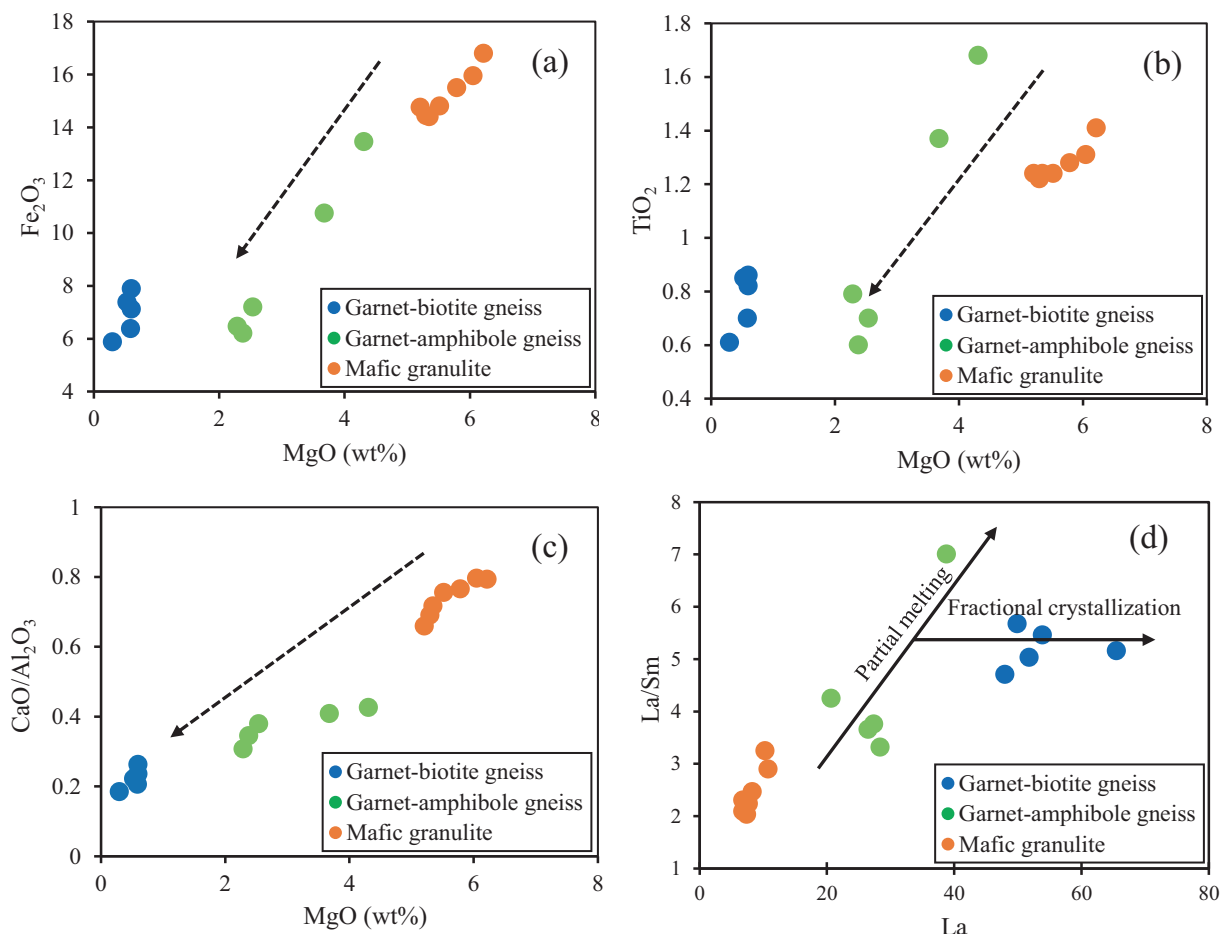


Fig. 9 Binary plots of selected major elements and ratio against SiO_2 and MgO (a, b, c). La/Sm vs. La binary plot of Blein et al. (2001) showing partial melting and crystal fractionation orientation (d)

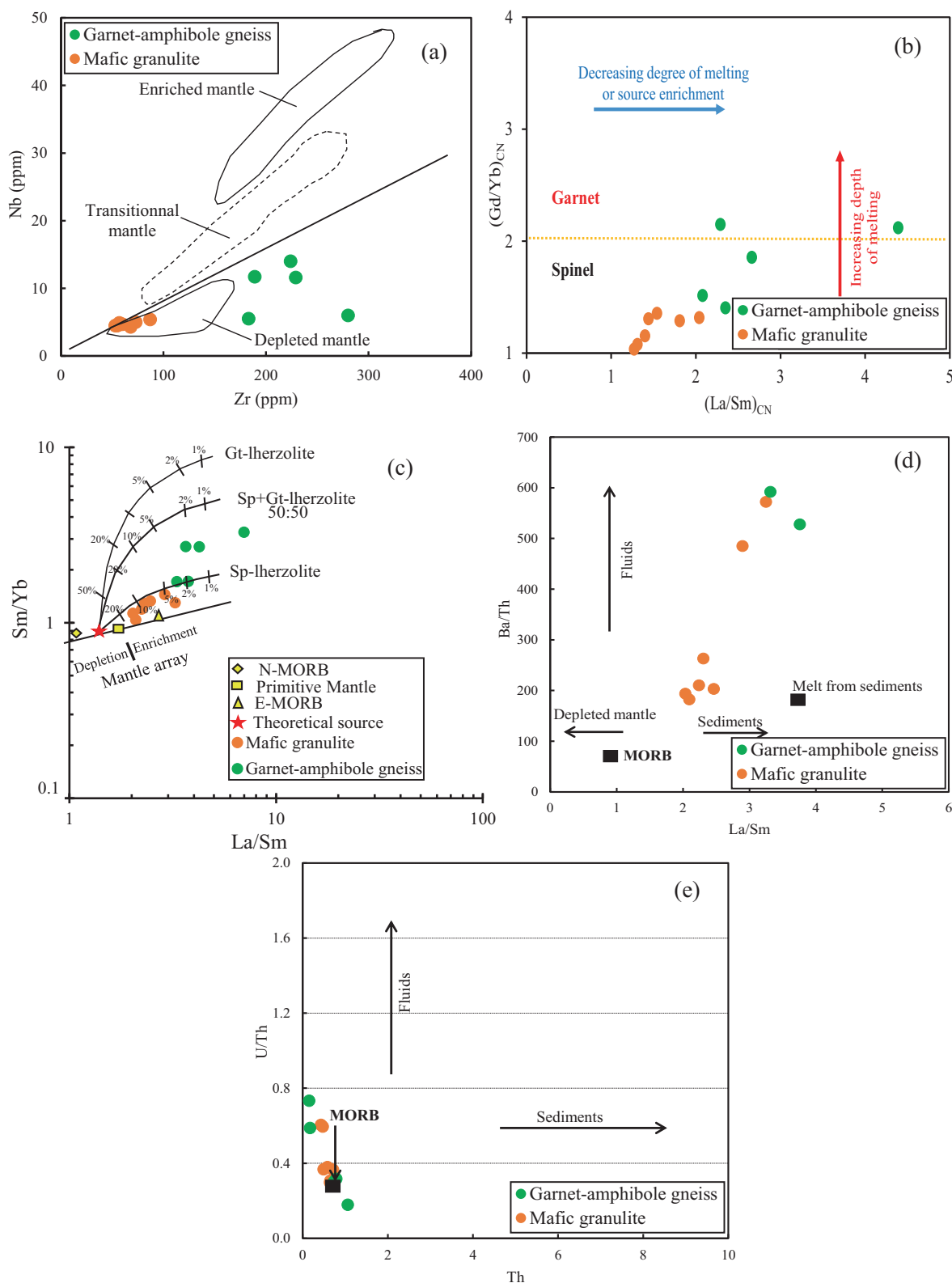


Fig. 10 **a** Zr-Nb diagram (Geng et al. 2011); **b** $(\text{Gd}/\text{Yb})_{\text{CN}}$ vs. $(\text{La}/\text{Sm})_{\text{CN}}$ plot indicating that the source of the studied metabasite rocks mainly originated from shallow melting depth. **c** La/Sm vs. Sm/Yb diagram (Alvaro et al. 2014) to determine the possible mantle source. Melt curves are drawn for spinel-lherzolite, garnet-lherzolite, and a 50:50 mixture of spinel- and garnet-lherzolite. Modal compositions of spinel-lherzolite (olivine 53 %, Opx 27 %, Cpx 17 %, spinel 3 %) and of garnet-lherzolite (olivine 60 %, Opx 20 %, Cpx 10 %, garnet 10 %) are after Kinzler (1997) and Walter (1998). Mineral/melt partition coefficients for basaltic liquids are after the compilation of Rollinson (1993). Primitive Mantle, N-MORB, E-MORB, and OIB compositions are from Sun and McDonough (1989). **e** Ba/Th - La/Sm diagram (Elliott 2003); and **f** U/Th - Th diagram (Dilek et al. 2008) for the Kribi metabasite rocks

(Fig. 10a), all the mafic granulite samples show very low Nb and Zr contents and plots in the field of depleted mantle source suggesting that the source is near the crust. In contrast, the garnet-amphibole gneiss samples exhibit relatively high Zr contents (mean = 221 ppm) and plot out of the mantle source. As discussed above, the geochemical compositions of the Kribi metabasite rocks revealed that some degree of crustal contamination and fractional crystallization influenced the differentiation of the source. Therefore, it becomes difficult to constrain their mantle source-derived primary magma composition. Zhang et al. (2012b) proposed a binary diagram based on REE to estimate the facies (garnet or spinel) and thus the depth of the magma source. On the Nb vs. Zr diagram (Fig. 10a), all the mafic granulite samples show very low Nb and Zr contents and plots in the field of depleted mantle source. In contrast, the garnet-amphibole gneiss samples exhibit relatively high Zr contents (mean = 221 ppm) and plot out of the mantle source. Many authors (e.g. Zhang et al. 2006, Rooney 2010; Alvaro et al. 2014 and references therein) have used REE ratio (e.g. Gd/Yb , Tb/Yb , La/Sm , Gd/Yb , Sm/Yb) to constrain the source of mafic magma. According to Rooney (2010), garnet-bearing source display $(\text{Gd}/\text{Yb})_{\text{N}} > 2$ or $(\text{Tb}/\text{Yb})_{\text{N}} > 1.8$. The average $(\text{Gd}/\text{Yb})_{\text{N}}$ ratio of the Kribi metavolcanic rocks is 1.21, suggesting that garnet was not involved in their source. This interpretation is consistent with the $(\text{Gd}/\text{Yb})_{\text{N}}$ vs. $(\text{La}/\text{Sm})_{\text{N}}$ diagram in which most of the studied samples plot in the spinel-bearing source field, suggesting shallow melting depth (Fig. 10b). Samples PGKR2 and KR7A of garnet-amphibole gneiss with $(\text{Gd}/\text{Yb})_{\text{N}}$ of 2.12 and 2.15, respectively plot in the field of the garnet-bearing source. Furthermore, Sm/Yb vs. La/Sm binary plot (Alvaro et al. 2014) was used to better investigate the mantle source and depth of melting. In this diagram (Fig. 10c), the metabasite rocks may have resulted from ca. 2–15 % of partial melting of spinel lherzolite with no garnet. Furthermore, except for sample KR7A with high Dy/Yb ratios (2.36) and slightly fractionated HREE

patterns, the studied metabasite rocks show flat HREE patterns and Dy/Yb ratios < 2 (mean: 1.67 and 1.96 for mafic granulite and garnet-amphibole gneiss respectively), confirming that there was no residual garnet in the peridotite mantle source (Jung et al. 2006). This finding suggests that spinel lherzolite source has participated in the genesis of the Kribi metabasite rocks, similar to that of the Eseka serpentized peridotite (Nga Essomba et al. 2020), the Mewengo amphibolites (Kwamou et al. 2021) within the Nyong Group, and the Anti-Atlas margin lava flows within the West African Craton (Álvaro et al. 2014).

To ascertain the processes affecting mantle source magma, Elliott (2003) argued that high Ba/Th and low La/Sm ratios are indicative of a mantle source altered by oceanic crustal fluids, and that low Ba/Th ratios are attributed to the melting of sediments. Dilek et al. (2008) suggested that high U/Th ratios are indicative of a mantle source magma that has been influenced by aqueous fluids. Consequently, the Ba/Th vs. La/Sm and U/Th vs. Th plots are widely used to gauge the influence of aqueous fluids and the contribution of subduction zone materials on the magma source (Fig. 10d and e). Three samples of garnet-amphibole gneiss samples (PGKR2, PGKR4, and KR7A) display very high Ba/Th ratios (2553, 793, and 3888, respectively) suggesting the significant influence of oceanic crust fluids, although they fall outside the scope of the Ba/Th vs. La/Sm diagram (Fig. 10d). On the U/Th vs. Th plot, both mafic granulite and garnet-amphibole gneiss samples exhibit the trend of aqueous fluids (Fig. 10e). The geochemical features also suggest that the amount of fluid may be limited for mafic granulite and more important for garnet-amphibole gneiss samples (Fig. 10e). Therefore, we suggest that the primary magma of the Kribi metabasite rocks derived from partial melting of metasomatized spinel peridotite source which has been subjected to various degrees of crystal fractionation and crustal contamination.

5.4.2 Genesis of metafelsic rocks

The magma of felsic rocks is commonly derived from three main mechanisms including (1) fractional crystallization process from basaltic or andesitic magma with or without crustal assimilation (DePaolo 1981), (2) partial melting of the crust, or (3) partial melting of the subducted oceanic crust (Huppert and Sparks 1988; Annen et al. 2006). From the field investigations, the Kribi metafelsic rocks (garnet-biotite gneiss) are spatially associated with garnet-amphibole gneiss and mafic granulite (Fig. 3), suggesting a genetic relationship. These rocks display a good correlation on binary plots with selected major elements against MgO (Fig. 9a, b, and c), suggesting that they are probably linked to each other through the fractional crystallization process. However, the garnet-biotite gneiss samples display calc-

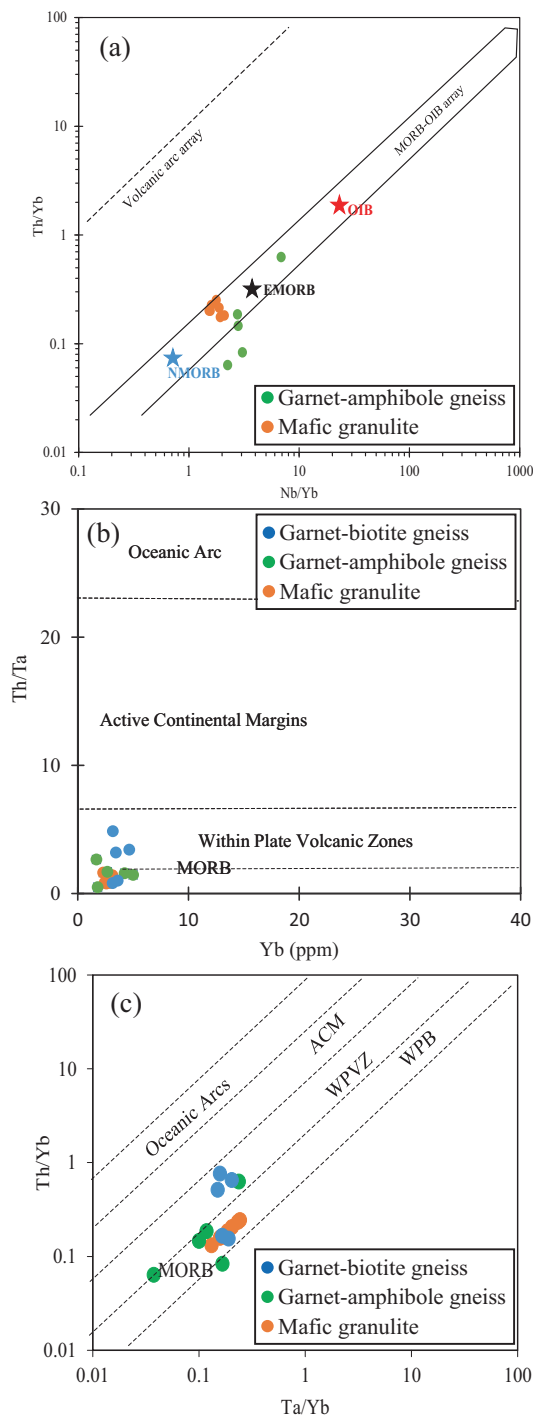


Fig. 11 Tectonic setting discrimination diagrams of the Kribi metavolcanic rocks. **a** Th/Yb vs. Nb/Yb diagram for mafic rocks (Pearce 2008) Geochemical data of NE Brazil metavolcanic rocks (Spreafico et al. 2019) are plotted for comparison. **b, c** Th/Ta vs. Yb and Th/Yb vs Ta/Yb, respectively (Schandl and Gorton 2002)

alkaline affinity while the garnet-amphibole gneiss shows transitional to calc-alkaline affinity, and mafic granulite samples belong to tholeiitic series (Fig. 7d). Depletions in P and Ti on their multielement diagram (Fig. 5e) are

attributed to fractionation of apatite and ilmenite (or rutile), respectively during petrogenesis. However, this depletion could also reflect the contribution of crustal contamination processes. On La/Sm vs. La diagram (Blein et al. 2001; Fig. 9d), in contrast to garnet-amphibole gneiss, the garnet-biotite gneiss samples show a more pronounced fractional crystallization trend indicating that only slight partial melting may have operated during igneous differentiation. Therefore, we suggest that the protolith of the metafelsic and metamafic rocks derived from a common parental magma, which was subjected to various degrees of partial melting, fractional crystallization, and crustal contamination (DePaolo 1981; Huppert and Sparks 1988).

5.5 Tectonic significance

Mantle plume is an alternative process that can explain the chemistry of the investigated metavolcanic rocks. Indeed, geochemistry data provides a useful tool for assessing which magmatic events are plume-related and for identifying changes in plume character with time (Erst and Buchan 2003). The arrival of mantle plumes from the deep mantle can be convincingly recognized through large volume-short duration (< 10 Ma) magmatic events, so-called large igneous provinces, LIPs. Such rocks commonly display the chemistry of ocean island basalts (OIBs). Uncontaminated plume-generated basaltic rocks should have flat REE patterns or LREE-enriched patterns and lack negative Nb, Ta, and Ti anomalies. The presence of high-MgO magmas (picrites and komatiites) is considered diagnostic of plumes. Such high-MgO magmas were not reported so far in the Nyong Group, except for serpentinized peridotite recently reported in the Eseka area (Nga Essomba et al. 2020). The Kribi mafic granulite samples display relatively flat NMORB-normalized REE patterns, with slight LREE enrichment; similar to OIB. However, these patterns show negative Nb, Ta, and Ti anomalies which is inconsistent with OIB chemistry. In addition, the REE patterns of garnet-amphibole gneiss and garnet-biotite gneiss are not flat and show negative anomalies in HFSE (Nb, P, and Ti), suggesting that the Kribi metavolcanic rocks are not the by-product of mantle plume.

Dissimilarities in the geochemical characteristics of volcanic rocks such as large ion lithophile (LILE), high field strength (HFSE), as well as rare earth elements (REE) from various tectonic settings have been an important tool in determining tectonic settings (Pearce and Cann 1973; Sun and McDonough 1989; Condie 2005). The Nb/Yb vs. Th/Yb diagram (Pearce 2008) is a useful diagram to constrain the geodynamic settings of the protolith of the mafic metavolcanic rocks. In the light of this diagram, the studied rocks plot in the mantle array and are clustered between N-MORB and E-MORB, similar to the NE Brazil

Table 4 Average whole rock major and trace elements geochemical composition of the São Francisco-Congo Paleοcontinent metavolcanic rocks

| Craton | Congo craton (CC) | | São Francisco craton (SFC) | | RMMS (Leal et al. 2021) | | RSC (De Paula Garcia et al. 2021) | | | | |
|--------------------------------|-------------------|--------------------|----------------------------|-------------------------|-------------------------|-----------------------|-----------------------------------|----------------------|-----------------------|--------------------|----------------------|
| | Petrology | Metabasalt (n = 7) | Meta-andesite (n = 5) | Metarhyodacite (n = 24) | Metabasalt (n = 24) | Meta-andesite (n = 1) | Metarhyodacite (n = 13) | Metabasalt I (n = 3) | Metabasalt II (n = 7) | Metabasalt (n = 7) | Metarhyolite (n = 4) |
| SiO ₂ | 50.6 | 60.1 | 68.6 | 51.2 | 57.24 | 77.8 | 52.43 | 49.4 | 52 | 73.4 | |
| Al ₂ O ₃ | 13.1 | 15.9 | 12.7 | 14.4 | 14.2 | 11.1 | 13.8 | 12.2 | 13.1 | 11.1 | |
| Fe ₂ O ₃ | 15.2 | 8.8 | 6.9 | 12.5 | 10.32 | 4 | 11.84 | 13 | 12.87 | 3.1 | |
| CaO | 9.7 | 5.9 | 2.8 | 9.8 | 8.5 | 0.5 | 10.9 | 10.7 | 7.2 | 0.2 | |
| MgO | 5.6 | 3.0 | 0.5 | 6.4 | 5.01 | 1 | 7.35 | 9.4 | 3.56 | 0.2 | |
| Na ₂ O | 3.0 | 4.0 | 2.8 | 2.0 | 2.57 | 3.4 | 2.06 | 1.8 | 1.2 | 3.1 | |
| K ₂ O | 0.4 | 0.8 | 3.3 | 0.3 | 0.74 | 2.4 | 0.39 | 0.7 | 1.64 | 3.7 | |
| TiO ₂ | 1.3 | 1.0 | 0.8 | 2.3 | 0.73 | 0.2 | 0.95 | 0.9 | 2.77 | 0.2 | |
| MnO | 0.2 | 0.1 | 0.1 | 0.6 | 0.16 | < 1 | 0.17 | 0.2 | 0.12 | 0 | |
| P ₂ O ₅ | 0.1 | 0.2 | 0.3 | 0.1 | 0.05 | < 1 | 0.07 | 0.01 | 0.4 | 0 | |
| Ba | 158.6 | 546.8 | 2832.0 | 137.4 | 136 | 647.1 | 33.7 | 92.3 | 559.8 | 431 | |
| Rb | 2.5 | 6.8 | 68.6 | 7.4 | 12.2 | 56.1 | 14.8 | 29.5 | 31.8 | 89 | |
| Sr | 142.3 | 432.2 | 338.2 | 129.7 | 112 | 64.2 | 113.7 | 96.3 | 703.8 | 575.7 | |
| Zr | 64.7 | 221.0 | 700.6 | 95.4 | 121 | 400 | 52 | 59.7 | 222.14 | 60 | |
| Nb | 4.8 | 9.8 | 13.3 | 4.6 | 2.85 | 19 | 2.4 | 8.2 | 18.7 | 38.2 | |
| Ta | 0.5 | 0.4 | 0.6 | 0.1 | 0.31 | 1.1 | 0.4 | 0.5 | 1.1 | 2.9 | |
| Th | 0.6 | 0.6 | 1.6 | 1.6 | 3.1 | 13 | 0.2 | 2.1 | 7.3 | 22.5 | |
| U | 0.2 | 0.2 | 0.6 | 0.5 | 1.08 | 3 | 0.14 | 0.4 | — | — | |
| Hf | 2.3 | 5.6 | 15.6 | 2.6 | 2.82 | 10.3 | 1.5 | 1.2 | — | — | |
| V | 387.0 | 172.4 | 27.4 | 340.0 | 313 | 63.3 | 249.3 | 206.4 | 233.1 | 5 | |
| Y | 27.3 | 33.0 | 37.3 | 26.9 | 20.78 | 58.4 | 18.5 | 23.1 | 28.2 | 60 | |
| Ti | 7656.3 | 6162.7 | 4604.0 | 26.9 | 6878.4 | 4380 | 1486.1 | 5674.4 | 16654.7 | 1453.5 | |
| La | 8.3 | 28.4 | 53.8 | 10.6 | 24.1 | 59.3 | 6.7 | 14.1 | 36.1 | 96 | |
| Ce | 18.5 | 60.3 | 108.6 | 21.2 | 30.9 | 0.5 | 7.8 | 22.3 | 72.6 | 177.3 | |
| Pr | 2.5 | 7.5 | 13.1 | 2.9 | 3.65 | 13 | 1.2 | 3.1 | 8.7 | 25.1 | |
| Nd | 11.6 | 31.6 | 53.7 | 12.9 | 14.2 | 50 | 6.2 | 13.6 | 36.8 | 91 | |
| Sm | 3.4 | 6.7 | 10.4 | 3.6 | 3.1 | 10 | 2 | 3.3 | 7.8 | 15.6 | |
| Eu | 1.1 | 1.5 | 3.6 | 1.2 | 0.83 | 1.6 | 0.8 | 1 | 2.4 | 2 | |
| Gd | 4.1 | 6.5 | 8.8 | 4.5 | 3.61 | 10 | 2.8 | 3.6 | 7.7 | 16 | |
| Tb | 0.7 | 1.0 | 1.2 | 0.8 | 0.56 | 1.6 | 0.5 | 0.6 | 1.1 | 2.1 | |
| Dy | 4.5 | 6.3 | 7.2 | 5.0 | 3.64 | 10.3 | 3.3 | 4.2 | 6.3 | 12.4 | |

Table 4 continued

| Craton | Congo craton (CC) | | | São Francisco craton (SFC) | | | RMMS (Leal et al. 2021) | RSC (De Paula Garcia et al. 2021) | | |
|---------------------------|-----------------------|--------------------------|---------------------------|------------------------------|--------------------------|----------------------------|-------------------------|-----------------------------------|-----------------------|-------------------------|
| | Kribi (This study) | | | MNGB (Spreafico et al. 2019) | | | | | | |
| Petrology | Metabasalt (n = 7) | Meta-andesite (n = 5) | Metarhyodacite (n = 5) | Metabasalt (n = 24) | Meta-andesite (n = 1) | Metarhyodacite (n = 13) | Metabasalt I (n = 3) | Metabasalt II (n = 7) | Metabasalt (n = 7) | Metarhyolite (n = 4) |
| Ho | 1.0 | 1.3 | 1.5 | 1.0 | 0.75 | 2.1 | 0.7 | 0.8 | 1.1 | 2.4 |
| Er | 2.8 | 3.5 | 4.0 | 3.1 | 2.17 | 6.4 | 2.1 | 2.5 | 3.2 | 7 |
| Tm | 0.4 | 0.5 | 0.6 | 0.4 | 0.35 | 1 | 0.3 | 0.4 | 0.4 | 1 |
| Yb | 2.7 | 3.1 | 3.6 | 2.9 | 2.1 | 6.3 | 2 | 2.5 | 2.72 | 6.4 |
| Lu | 0.4 | 0.4 | 0.6 | 0.4 | 0.33 | 1 | 0.3 | 0.3 | 0.4 | 0.8 |
| Nb/Y | 0.2 | 0.3 | 0.4 | 0.2 | 0.14 | 0.4 | 1.3 | 0.4 | 0.6 | 0.6 |
| Zr/Ti | 0.0 | 0.0 | 0.2 | 0.0 | 0.03 | 0.3 | 0 | 0 | 0 | 0 |
| Nb/Yb | 1.8 | 3.5 | 3.7 | 1.6 | 1.36 | 3.6 | 1.3 | 4.1 | 6.8 | 6 |
| Th/Yb | 0.2 | 0.2 | 0.4 | 0.5 | 1.48 | 2.5 | 0.14 | 0.9 | 2.5 | 3.5 |
| (La/ Sm) _{CN} | 1.5 | 2.8 | 3.3 | 1.8 | 5.02 | 4 | 2.2 | 3 | 3 | 4 |
| (Gd/ Yb) _{CN} | 1.2 | 1.8 | 2.0 | 1.3 | 1.42 | 1.4 | 1.2 | 1.3 | 3 | 2.1 |

MNGB Mundo Novo greenstone belt, RMMS Riacho dos Machados metavolcanosedimentary sequence, RSC Rio Salitre Complex

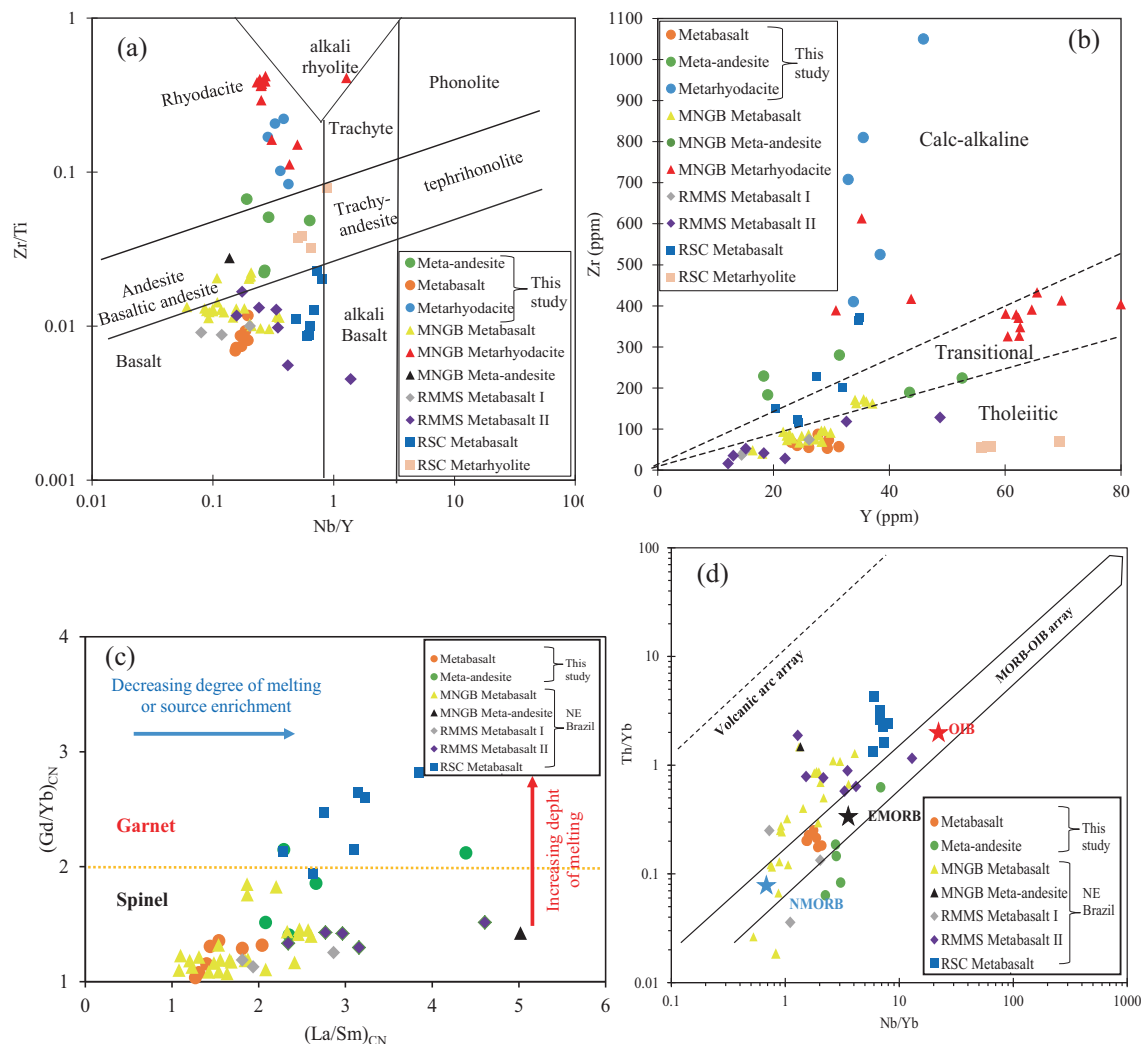


Fig. 12 Whole-rock geochemical binary diagrams showing the comparison between the São Francisco craton and Congo craton metavolcanic rocks. **a** Zr/TiO₂ vs. Nb/Y; **b** Zr vs. Y; **c** (Gd/Yb)_{CN} vs. (La/Sm)_{CN}; **d** Th/Yb vs. Nb/Yb diagram for mafic rocks. MNGB: Mundo Novo greenstone belt; RMMS: Riacho dos Machados meta-volcano sedimentary sequence; RSC: Rio Salitre Complex

metavolcanic rocks (Fig. 11a). In addition, a series of tectonic discrimination diagrams (Fig. 11b–c), which are appropriate for magmas of intermediate-felsic composition, were used to confirm their paleotectonic environment (Pearce 1982; Schandl and Gorton 2002). According to Pearce (1982), within-plate lavas are Ti- and Zr-enriched compared to the volcanic arc lavas. Therefore, this author proposed the use of Ti vs. Zr plot for discrimination of volcanic arc and within-plate settings. On the other hand, Schandl and Gorton (2002) suggested the use of immobile HFSE (e.g. Ta, Yb, Th, and Hf) to discriminate oceanic arc, active continental margin, and within-plate volcanic zone magmas. On the Yb vs. Th/Ta diagram, the investigated metavolcanic rocks plot mainly in the within-plate volcanic zones setting (Fig. 11b). This tectonic environment is also suggested by the Th/Yb vs. Ta/Yb plot (Fig. 11c) in which the mafic granulite and garnet-amphibole gneiss samples

are concentrated in the within-plate basalts field, while garnet-biotite gneiss samples show the tendency of both within-plate basalts (two samples) and within-plate volcanic zones (three samples) lavas. Therefore, the Kribi metavolcanic rocks mostly bear the characteristics of within-plate lavas, suggesting an extensional tectonic environment.

5.6 Possible equivalents of the investigated metavolcanic rocks in other parts of the Ntem Complex and São Francisco craton

5.6.1 Comparison with Ntem complex metavolcanic rocks

The occurrence of well-preserved metavolcanic rocks has been reported in numerous areas within the Ntem Complex and interpreted as remnants of the greenstone belts. The

Nyong Group greenstone belt with NNE-SSW trend is well-exposed along the Eséka-Lolodorf-Kribi road and includes epidosites, amphibolites, mafic granulites, pyroxenites, serpentinites, and eclogites. All these metavolcanic rocks are dominantly basaltic to basaltic-andesite in composition and belong to tholeiitic and calc-alkaline series with MORB-like geotectonic settings Bouyo Houketchang et al. 2019; Moudioh et al. 2020; Kwamou et al. 2021) similar to the Kribi metabasite rocks. The protolith of the Kribi metavolcanic rocks crystallized during Neoarchean at 2671 ± 51 Ma (96.5 % conf., n = 15) and metamorphosed up to granulite facies at 2065 ± 55 Ma (95 % conf., n = 10). In the Nyong Group, Archean tholeiitic magmatism was reported at Lolordorf (Owona et al. 2020b) and Boumnyebel (Nkoumbou et al. 2015) areas. This magmatism is mainly represented by amphibolite with basalt to basaltic-andesite composition and MORB signature. The protolith of the Lolordorf amphibolite crystallized at 2819 Ma and experienced metamorphism/recrystallization during both Paleoproterozoic (2054 Ma) and Neoproterozoic (730 Ma) times (Owona et al. 2020b). In the Boumnyebel area, Nkoumbou et al. (2015) documented Mesoarchean (2776 Ma) age for the amphibolite. This age is quite similar to the upper intercept age of 2779 Ma of the Kribi metavolcanic rocks. On the other hand, tholeiitic magmatism in the Ntem Group was constrained at 2628 Ma using the whole-rock Rb-Sr method (Tchameni et al. 1995). In addition, previous studies have revealed that Neoarchean magmatism is also responsible for the emplacement of high-K granitoids (ca. 2722 Ma, ca. 2666 Ma) for Sangmelima and Ebolowa high-K granites, respectively (Tchameni et al. 2000). The Neoarchean protolith age obtained in the present study suggests temporal relationships between the Kribi metavolcanic rocks and both tholeiitic and high-K magmatism, and thus bimodal Neoarchean magmatism within the Ntem Complex. 2065 ± 55 Ma metamorphic ages reported in this work falls within the ca. 2100–2000 Ma high-grade tectono-metamorphic event widely documented in the Ntem Complex and attributed to Eburnean/Trans-Amazonian orogeny imprints Toteu et al. 1994; Lerouge et al. 2006; Owona et al. 2020, 2021; Nzepang Tankwa et al. 2021, Soh Tamehe et al. 2021).

5.6.2 Comparison with São Francisco craton metavolcanic rocks

The São Francisco craton (SFC) together with its African counterpart (Congo craton) constitute the São Francisco-Congo Paleocontinent SFCP (Almeida et al. 1977; Heilbron et al. 2017). The Nyong Group, which is part of the CC in Cameroon has been reworked during the Eburnean orogeny coeval to widespread high-grade metamorphism at

ca. 2.05 Ga Toteu et al. 1994; Lerouge et al. 2006; Owona et al. 2020, 2021; Nzepang Tankwa et al. 2021, Soh Tamehe et al. 2021). Within the SFC, the Trans-Amazonian orogeny and high-grade metamorphism were also reported within the same period (Barbosa and Sabaté 2004; Neves et al. 2006). This orogeny is generally interpreted as resulting from the collision /assemblage between the SFC and CC (Almeida et al. 1977; Neves et al. 2006; Heilbron et al. 2017). The SFC is divided into two main parts. The northern part comprising four crustal blocks (Jequié, Gavião, Serrinha and Itabuna-Salvador-Curaça), and the southern part consisting of greenstone belts and gneissic complexes Barbosa and Sabaté 2004; Moreno et al. 2017; De Paula Garcia et al. 2021 and references therein). Whole-rock geochemical data of some metavolcanic rocks from both northern and southern parts, including metabasalt, meta-andesite, metarhyolite and metadacite rocks (Spreafico et al. 2019; Leal et al. 2021; De Paula Garcia et al. 2021) were used for comparison (Table 4). On the Zr/TiO₂ vs. Nb/Y (Winchester and Floyd 1977) discrimination diagram, the metabasite (mafic granulite and garnet-amphibole gneiss) and metafelsic rocks (biotite-amphibole gneiss) from this study likewise mafic and felsic rocks from the SFC plot within the basalt, basalt-andesite, and rhyodacite field respectively (Fig. 12a). In the Zr vs. Y diagram of MacLean and Barrett (1993), the SFC and the CC metavolcanic rocks display tholeiitic to calc-alkaline affinity (Fig. 12b). The metabasalt samples from both SFC and CC generally exhibit a tholeiitic affinity, except the Rio Salitré Complex (RSC) metabasalt rocks within the SFC which are transitional to calc-alkaline. On the (Gd/Yb)_{CN} vs. (La/Sm)_{CN} diagram, all the metabasalt samples fall in the spinel peridotite field, except the RSC metabasalt samples which plot in the garnet peridotite zone indicating the deeper depth of the mantle source (Fig. 12c). The Kribi metabasite rocks mainly show MORB-like features. In contrast, the SFC metabasalts generally present back-arc characteristics, excluding a few samples which fall between and below the mantle array, suggesting that metamorphism/metasonatism has affected those samples (Fig. 12d). The Kribi metarhyodacite rocks yielded average Pb-Pb age of 2067 ± 55 Ma, consistent with the Eburnean/Trans-Amazonian orogeny, suggesting a similar paleotectonic scenario on both sides of the south Atlantic during Paleoproterozoic times. However, further investigations (tectonics, geochemical, and geochronology) are necessary for a better comparison between these two Archean cratonic blocks (SFC and CC) and to reconstruct their assemblage at ca. 2.05 Ga.

6 Conclusions

Integrated field investigations, whole-rock geochemistry, and LA-ICP-MS zircon U-Pb data of the Kribi metavolcanic rocks support the following conclusions:

- (1) The Kribi metavolcanic rocks include mafic granulite, garnet-amphibole gneiss and garnet-biotite gneiss. They occur interband with metasediments and have experienced granulite facies metamorphism and polyphase deformation.
- (2) They display basalt (mafic granulite), basaltic andesite (garnet-amphibole gneiss) to rhyodacite rocks (garnet biotite gneiss) compositions, low-to medium-K subalkaline, and metaluminous.
- (3) They show tholeiitic to calc-alkaline affinity, MORB-like, and within-plate setting geochemical signatures. These features are compatible with oceanic volcanism in an extensional tectonic environment.
- (4) The metabasite rocks (basalt to basaltic andesite protolith) are likely the equivalent of a spinel peridotite product representing $\sim 2\text{--}15\%$ partial melting of metasomatized mantle source, while the metarhyodacite rocks are derived from a common parental magma, which was subjected to various degrees of fractional crystallization.
- (5) The rhyodacite rocks display a crystallization age of 2671 ± 51 Ma (Neoarchean) and were metamorphosed at 2065 ± 55 Ma (Paleoproterozoic). About regional geochronology, the Neoarchean protolith age is comparable to the ca. 2628 Ma tholeiitic magmatism and ca. 2666 Ma high-K granites, suggesting the occurrence of bimodal Neoarchean magmatism within the Ntem Complex. 2065 ± 55 Ma metamorphic ages fall within the ca. 2100–2000 Ma high-grade tectono-metamorphic event attributed to Eburnean/Trans-Amazonian orogeny imprints.
- (6) At the regional scale, metavolcanic rocks with comparable geochemical and geochronological characteristics are documented in the São Francisco Craton (SFC) in Brazil, suggesting similar geodynamic evolution on both sides of the south Atlantic during the Paleoproterozoic.

Acknowledgements The data presented in this paper represent part of the Ph.D thesis of the first author at the Department of Earth Sciences of the University of Yaounde I. The authors are greatly indebted to Dr Landy Soh Tamehe of the School of Geosciences and Info-Physics, Central South University, China for helping in zircon U-Pb data acquisition. This research did not receive any specific grant from funding agencies in the public, commercial, or not-for-profit

sectors. The authors are indebted to Prof. Li Huan and two anonymous reviewers for their thoughtful and constructive comments.

Declarations

Conflict of interest On behalf of all authors, the corresponding author states that there is no conflict of interest.

References

- Almeida FFM (1977) O cráton do São Francisco. Revista Brasileira de Geociências 7:349–364
- Álvaro JJ, Pouclet A, Ezzouhairi H, Souleymani A, Bouougri E, Imaze H, Fekkak AG (2014) Early Neoproterozoic rift-related magmatism in the Anti-Atlas margin of the West African craton, Morocco. Precambrian Res 255:433–442
- Annen C, Blundy JD, Sparks RSJ (2006) The genesis of intermediate and silicic magmas in deep crustal hot zones. J Petrol 47:505–539
- Barbosa JS, Barbosa RG (2017) The Paleoproterozoic eastern bahia orogenic domain. In: Heilbron M, Cordani UG, Alkmim FF (Eds) São Francisco Craton, Eastern Brazil. Tectonic Genealogy of a Miniature Continent. Springer, pp 57–69
- Barbosa JSF, Sabaté P (2004) Archean and Paleoproterozoic crust of the São Francisco Craton, Bahia, Brazil: geodynamic features. Precambrian Res 133(1–2):1–27. <https://doi.org/10.1016/j.precamres.2004.03.001>
- Belousova E, Griffin W, O'Reilly SY, Fisher N (2002) Igneous zircon: trace element composition as an indicator of source rock type. Contrib Miner Petrol 143:602–622
- Beuchert MJ, Podladchikov YY, Simon NSC, Rüpké LH (2010) Modeling of craton stability using a viscoelastic rheology. J Phys Res 115:B11413
- Blein O, Lapierre H, Schweickert RA (2001) A Permian island-arc with a continental basement: the Black Dyke Formation Nevada, North American Cordillera. Chem Geol 175:543–566. [https://doi.org/10.1016/S0009-2541\(00\)00357-0](https://doi.org/10.1016/S0009-2541(00)00357-0)
- Bouyo Houketchang M, Penaye J, Mouri H, Toteu SF (2019) Eclogite facies metabasites from the Paleoproterozoic Nyong Group, SW Cameroon: Mineralogical evidence and implications for a high-pressure metamorphism related to a subduction zone at the NW margin of the Archean Congo craton. J Afr Earth Sc 149:215–234
- Chombong NN, Suh CE, Lehmann B, Vishiti A, Ilouga DC, Shemang EM, Tantoh BS, Kedia AC (2017) Host rock geochemistry, texture and chemical composition of magnetite in iron ore in the Neoarchean Nyong unit in southern Cameroon. Appl Earth Sci 126:129–145
- Condie KC (2005) High field strength element ratios in *Archean basalts*: a window to evolving sources of mantle plumes? Lithos 79:491–504
- Currie C, Van Wijk J (2016) How craton margins are preserved: Insights from geodynamic models. J Geodyn 100:144–158
- Dai LQ, Zhao ZF, Zheng YF, Li Q, Yang Y, Dai M (2011) Zircon Hf-O isotope evidence for crust–mantle interaction during continental deep subduction. Earth Planet Sci Lett 308:229–244
- DePaolo DJ (1981) Trace element and isotopic effects of combined wall rock assimilation and fractional crystallization. Earth Planet Sci Lett 53:189–202
- De Paula Garcia PM, Carrilho ELuizV, Ribeiro LVC, Misi BP, Da Silva A, Correia SJH, Rios D (2021) Geology, petrogenesis, and geochronology of the Rio Salitre Complex: implications for the Paleoproterozoic evolution of the northern São Francisco Craton, Brazil. J S Am Earth Sci 107:103112

- Djoukouo Soh AP, Ganno S, Zhang LC, Soh Tamehe L, Wang CL, Peng ZD, Tong XX, Nzenti JP (2021) Geochemical and geochronological constraints on the origin of the Bibole banded iron formations, northwestern Congo Craton, Cameroon: implications for their depositional age and tectonic environment. *Geol Mag* 158:2245–2263. <https://doi.org/10.1017/S0016756821000765>
- Dilek Y, Furnes H, Shallo M (2008) Geochemistry of the Jurassic Mirdita Ophiolite (Albania) and the MORB to SSZ evolution of a marginal basin oceanic crust. *Lithos* 100:174–209
- Elliott T (2003) Tracers of the slab. In: Eiler J (ed) Inside the Subduction Factory. AGU, Washington, DC, pp 23–45
- Fahmi H, Yanuardi SN, Cendi DPD, Anastasia DT (2019) Geology and petrogenesis of igneous rocks from Batur Paleovolcano, Gunungkidul, Yogyakarta: evidence from their textures, mineralogy, and major elements geochemistry. *J Appl Geol* 4(1):32–42
- Feybesse JL, Johan V, Maurizot P, Abessolo A (1986) Mise en évidence d'une nappe syn métamorphe d'âge Eburnéen dans la partie NW du craton Zairois (SW Cameroun). Publication occasionnelle-Centre international pour la formation et les échanges géologiques, pp 105–111
- Feybesse JL, Johan V, Triboulet C, Guerrot C, Mayaga-Mikolo F, Bouchet V, Eko N J (1998) The West Central African belt: a model of 2.5–2.0 Ga accretion and two-phase orogenic evolution. *Precambrian Res* 87:161–216
- Fuanya C, Temidayo BA, Kankeu B, Fouateu YR, Tangko TE, Yetedje NF (2019) Geochemical characteristics and petrogenesis of basic rocks in the Ako'ozam-Njabilobe area, Southwestern Cameroon: implications for Au genesis. *SN Appl Sci* 1:904
- Ganno S, Moudioh C, Nchare NA, Nono K, Nzenti GD, J.P (2015) Geochemical fingerprint and iron ore potential of the siliceous itabirite from Palaeoproterozoic Nyong Series, Zambi area, southwestern Cameroon. *Resour Geol* 66(1):71–80
- Ganno S, Njiosseu Tanko EL, Nono K, Djoukouo Soh GD, Moudioh A, Ngnotué C, Nzenti T, J.P (2017) A mixed seawater and hydrothermal origin of Superior-type banded iron formation (BIF)-hosted Kouambo iron deposit, Palaeoproterozoic Nyong Series, Southwestern Cameroon: Constraints from petrography and geochemistry. *Ore Geo Rev* 80:860–875
- Ganno S, Tsozue D, Nono K, Tchouatcha GD, Ngnotué MS, Takam T, Nzenti GR, J. P (2018) Geochemical constraints on the origin of banded iron formation-hosted iron ore from the Archaean Ntem Complex (Congo Craton) in the Meyomessi area, southern Cameroon. *Resour Geol* 68(3):287–302
- Garrels RM, Mackenzie FT (1971) Evolution of sedimentary rocks. WW Norton and Company Inc., New York
- Geng H, Sun M, Yuan C, Zhao G, Xiao W (2011) Geochemical and geochronological study of early Carboniferous volcanic rocks from the West Junggar: petrogenesis and tectonic implications. *J Asian Earth Sci* 42:854–866
- Gerya T (2014) Precambrian geodynamics: concepts and models. *Gondwana Res* 25:442–463
- Gibson HL, Watkinson DH, Comba CDA (1983) Silicification; hydrothermal alteration in an Archean geothermal system within the Amulet Rhyolite Formation, Noranda, Quebec. *Econ Geol* 78:954–971
- Green TH, Pearson NJ (1986) Ti-rich accessory phase saturation in hydrous mafic-felsic compositions at high P. *T Chem Geol* 54:185–201
- Heilbron M, Cordani UG, Alkmim FF (eds) (2017) São Francisco Craton, eastern Brazil: Tectonic genealogy of a miniature continent. Springer, p 331
- Hoffmann JE, Münker C, Polat A, KönSchalteggerig S, Mezger K, Rosing MT (2010) Highly depleted Hadean mantle reservoirs in the sources of early Archean arc-like rocks, Isua supracrustal belt, southern west Greenland. *Geochim Cosmochim Acta* 74:7236–7260
- Hou KJ, Li YH, Tian YY (2009) In situ U-Pb zircon dating using laser ablation-multi ion counting-ICP-MS. *Mineral Deposits* 28(4):481–492 (in Chinese with English abstract)
- Huppert HE, Sparks RSJ (1988) The generation of granitic magmas by intrusion of basalt into continental crust. *J Petrol* 29:599–624
- Irvine TN, Baragar WRA (2011) A guide to the chemical classification of the Common volcanic rocks. *Can J Earth Sci* 8(5):158. <https://doi.org/10.1139/e11-055>
- Jung C, Jung S, Hoffer E, Berndt J (2006) Petrogenesis of Tertiary mafic alkaline magmas in the Hocheifel. *Ger J Petrol* 47(8):1637–1671
- Kankeu B, Greiling RO, Nzenti JP, Ganno S, Danguene PYE, Bassahak J, Hell J (2018) Contrasting Pan-African structural styles at the NW margin of the Congo Shield in Cameroon. *J Afr Earth Sc* 146:28–47
- Keppler H (1996) Constraints from partitioning experiments on the composition of subduction-zone fluids. *Nature* 380:237–240
- Kinzler RJ (1997) Melting of mantle peridotite at pressures approaching the spinel to garnet transition: application to mid-ocean ridge basalt petrogenesis. *J Geophys Res* 102:853–874
- Klein EM, Langmuir CH (1987) Global correlations of ocean ridge basalt chemistry with axial depth and crustal thickness. *J Geophys Res Solid Earth* 92:8089–8115
- Kwamou WMM, Nono K, Nkouathio GD, Kenne DGA, P (2021) Petrogenesis and U-Pb zircon dating of amphibolite in the Mewengo iron deposit, Nyong series, Cameroon: fingerprints of iron depositional geotectonic setting. *Arab J Geosci* 14:872
- Lasserre M, Soba D (1976) Age libérien des granodiorites et des gneiss à pyroxènes du Cameroun méridional. *Bull du BRGM* 2:17–32
- Leal VLS, Kuchenbecker Barbuena MD, Queiroga G (2021) Geochemistry and U-Pb zircon ages of the metamafic-ultramafic rocks of the Riacho dos Machados metavolcanosedimentary sequence: evidence of a late Rhyacian back-arc basin during the assembly of São Francisco-Congo paleocontinent. *J Pre-proof* 2:1068
- Ledru P, Eko Ndong JE, Johan V, Prian JP, Coste B, Haccard D (1989) Structural and metamorphic evolution of the Gabon orogenic belt: collision tectonics in the lower Proterozoic? *Precambrian Res* 44:227–241
- Lerouge C, Cocherie A, Toteu SF, Penaye J, Milési JP, Tchameni R, Nsifa EN, Fanning M, Deloule E (2006) Shrimp U-Pb zircon age evidence for Paleoproterozoic sedimentation and 2.05Ga syntectonic plutonism in the Nyong Group, South-Western Cameroon: consequences for the Eburnean–Transamazonian belt of NE Brazil and Central Africa. *J Afr Earth Sc* 44:413–427
- Loose D, Schenk V (2018) 2.09 Ga old eclogites in the Eburnian–Transamazonian orogen of southern Cameroon: significance for Palaeoproterozoic plate tectonics. *Precambrian Res* 304:1–11
- Ludwig KR (2003) Isoplot 3.00: a geochronological toolkit for Microsoft excel, Berkeley (CA), Berkeley Geochronology Center Special Publication, No. 4, p 70
- MacLean WH, Barrett TJ (1993) Lithochemical techniques using immobile elements. *J Geochem Explor* 48:109–133
- Maurizot P, Abessolo A, Feybesse JL, Lecomte PJ (1986) Etude de prospection minière du Sud-Ouest Cameroun: Synthèse des travaux de 1978 à 1985. Rapport BRGM 85, CMR 066
- Middelburg JJ, Van der Weijden CH, Woittiez JR (1988) Chemical processes affecting the mobility of major, minor and trace elements during weathering of granitic rocks. *Chem Geol* 68:253–273
- Miyashiro A (1974) Volcanic rock series in island arcs and active continental margins. *Am J Sci* 274:321–355

- Moreno JA, Baldim MR, Semprich J, Oliveira EP, Verma SK, Teixeira W (2017) Geochronological and geochemical evidences for extension-related Neoarchean granitoids in the southern São Francisco Craton, Brazil. *Precambrian Res* 294:322–343
- Moudioh C, Tamehe LS, Ganno S, Nzepang Tankwa M, Soares B, Ghosh M, Kankeu R, Nzentji BJP (2020) Tectonic setting of the Bipindi greenstone belt, northwest Congo craton, Cameroon: implications on BIF deposition. *J Afr Earth Sc* 171:103971
- Ndema Mbongue JL, Ngnotue T, Nlend N, Nzentji CD, Suh JPC, E (2014) Origin and evolution of the formation of the Cameroon Nyong Series in the western border of the Congo Craton. *J Geosci Geomatics* 2:62–75
- Nedelec A, Minyem D, Barbey P (1993) High-P/high-T anatexis of Archaean tonalitic grey gneisses: the Eseka migmatites, Cameroon. *Precambrian Res* 62:191–205
- Nedelec A, Nsifa EN, Martin H (1990) Major and trace element geochemistry of the Archaean Ntem plutonic complex (South Cameroon): petrogenesis and crustal evolution. *Precambrian Res* 47:35–50
- Neves SP, Bruguier O, Vauchez A, Bosch D, Silva JMR, Mariano G (2006) Timing of crust formation, deposition of supracrustal sequences, and Transamazonian and Brasiliano metamorphism in the East Pernambuco belt (Borborema Province, NE Brazil): implications for western Gondwana assembly. *Precambrian Res* 149:197–216
- Nga Essomba TP, Ganno S, Tanko Njiosseu EL, Mbongue N, Woguia JK, Tamehe BSoh, Wambo LTakodjou, Nzentji JD, J. P (2020) Geochemical constraints on the origin and tectonic setting of the serpentinized peridotites from the Paleoproterozoic Nyong series, Eseka area, SW Cameroon. *Acta Geochim* 39:404–422
- Niu Y, O'Hara MJ (2008) Global correlations of Ocean ridge Basalt chemistry with axial depth: a new perspective. *J Petrol* 49:633–664
- Niu Y, Regelous M, Wendt II, Batiza R, O'Hara MJ (2002) Geochemistry of near-EPR seamounts: importance of source vs process and the origin of enriched mantle component. *Earth Planet Sci Lett* 199:327–345
- Nkoumbou C, Barbey P, Yonta-Ngouné C, Paquette JL, Villiéras F (2015) Pre-collisional geodynamic context of the southern margin of the Pan-African Fold Belt in Cameroon. *J Afr Earth Sc* 99:245–260
- Nsifa Nkonguin E, Tchameni R, Nédélec A, Siqueira R, Pouplet A, Bascou J (2013) Structure and petrology of Pan-African nepheline syenites from the South West Cameroon; Implications for their emplacement mode, petrogenesis and geodynamic significance. *J Afr Earth Sc* 87:44–58
- Nzepang Tankwa M, Ganno S, Okunlola OA, Njiosseu T, Tamehe ELS, Woguia LKamguia, Mbita BMotto, Nzentji JP (2021) Petrogenesis and tectonic setting of the Paleoproterozoic Kelle Bidjoka iron formations, Nyong group greenstone belts, southwestern Cameroon. Constraints from petrology, geochemistry, and LA-ICP-MS zircon U-Pb geochronology. *Int Geol Rev* 63(14):1737–1757
- Owona S, Ondoja JM, Tichomirowa M, Ekodeck GE (2020a) The petrostructural characteristics and $^{207}\text{Pb}/^{206}\text{Pb}$ zircon data from the Ngomedzap-Akongo area (Nyong complex, SW-Cameroun). *J Geosci* 65:201–219
- Owona S, Ratschbacher L, Azfal MG, Nsangou Ngapna M, Mvondo Ondoja J, Ekodeck GE (2020) New U-Pb zircon ages of Nyong Complex meta-plutonites: implications for the Eburrean/Trans-Amazonian Orogeny in southwestern Cameroon (Central Africa). *Geol J* 56:1741–1755
- Owona S, Ratschbacher L, Nsangou Ngapna M, Gulzar AM, Ondoja M, Ekodeck J, G. E (2021a) How diverse is the source? Age, provenance, reworking, and overprint of Precambrian meta-sedimentary rocks of West Gondwana, Cameroon, from zircon U-Pb geochronology. *Precambrian Res* 359:106220
- Owona S, Ratschbacher L, Nsangou Ngapna M, Gulzar AM, Ondoja M, Ekodeck J, G. E (2021b) Reply to comment on “How diverse is the source? Age, provenance, reworking, and overprint of Precambrian meta-sedimentary rocks of West Gondwana, Cameroon, from zircon U-Pb geochronology” by Mvondo and Bineli Betsi”. *Precambrian Res* 366:106418
- Pearce JA (2008) Geochemical fingerprinting of oceanic basalts with applications to ophiolite classification and the search for Archean oceanic crust. *Lithos* 100:14–48
- Pearce JA, Cann JR (1973) Tectonic setting of basic volcanic rocks determined using trace element analyses. *Earth Planet Science Letter* 19:290–300
- Pearce JA (1982) Trace element characteristics of lavas from destructive plate boundaries. In: Thorpe RS (ed) *Andesites*. Wiley, Chichester, pp 525–548
- Pearce JA, Harris NBW, Tindle AG (1984) Trace element discrimination diagrams for the tectonic interpretation of granitic rocks. *J Petrol* 25:956–983
- Pearce JA, Peate DW (1995) Tectonic implications of the composition of volcanic ARC magmas. *Annual Rev Earth Planet Sci* 23:251–285
- Penaye J, Toteu SF, Tchameni R, Van Schmus WR, Tchakounté J, Ganwa A, Minyem D, Nsifa EN (2004) The 2.1Ga West Central African Belt in Cameroon: extension and evolution. *J Afr Earth Sc* 39:159–164
- Penaye J, Toteu SF, Michard A, Van Schmu WR, Nzentji JP (1993) U-Pb and Sm-Nd preliminary geochronologic data on the Yaoundé serie, Cameroon: reinterpretation of granulitic rock as the suture of the collision in the Centrafricain belt. *Rep Sci Acad* 317:789–794
- Polat A, Hofmann AW, Rosing MT (2002) Boninite-like volcanic rocks in the 3.7–3.8 Ga Isua greenstone belt, West Greenland: geochemical evidence for intra-oceanic subduction zone processes in the early Earth. *Chem Geol* 184:231–254
- Polat A, Regelous M, Hofmann AW, Appel PWU (2000) Contrasting geochemistry in the 3.7–3.8 Ga pillow basalt rims and cores, Isua greenstone belt, Greenland: implications for early Archean sea-floor alteration processes. *AGU EOS Trans.* 81:F1256
- Pouplet A, Tchameni R, Mezger K, Vidal M, Nsifa EN, Shang CK, Penaye J (2007) Archean crustal accretion at the northern border of the Congo craton (South Cameroon), The charnockite-TTG link. *Bull Geol Soc France* 178:331–342
- Rooney TO (2010) Geochemical evidence of lithospheric thinning in the southern Main Ethiopian Rift. *Lithos* 117:33–48
- Rollinson H (1993) Using geochemical data: evaluation, presentation, interpretation. Longman Group UK Ltd., Longman, p 352
- Rudnick RL, Fountain DM (1995) Nature and composition of the continental crust: a lower crustal perspective. *Rev Geophys* 33:267–309
- Schaltegger U, Fanning CM, Günther D, Maurin JC, Schulmann K, Gebauer D (1999) Growth, annealing and recrystallization of zircon and preservation of monazite in high-grade metamorphism: conventional and in-situ U/Pb isotope, cathodoluminescence and microchemical evidence. *Contrib minéralogie Petrol* 134:186e201
- Schandl ES, Gorton MP (2002) Application of high field strength elements to discriminate tectonic settings in VMS environments. *Econ Geol* 97:629–642
- Soh Tamehe L, Wei C, Ganno S, Rosiere CA, Nzentji JP, Ebotehoua CG, Lu G (2021) Depositional age and tectonic environment of the Gouap banded iron formations from the Nyong group, SW Cameroon: Insights from isotopic, geochemical and geochronological studies of drillcore sample. *Geosci Front* 12:549–572

- Spreafico RR, Barbosa F, Barbosa JS, Vitória de Moraes NS, A. M (2019) Tectonic evolution of the Neoproterozoic Mundo Novo greenstone belt, eastern São Francisco Craton, NE Brazil: Petrology, U-Pb geochronology, and Nd and Sr isotopic constraints. *J S Am Earth Sci* 95:102296. <https://doi.org/10.1016/j.james.2019.102296>
- Suh CE, Cabral A, Shemang EM, Mbinkar L, Mboudou GGM (2008) Two contrasting iron-ore deposits in the Precambrian mineral belt of Cameroon, West Africa. *Explor Mineral Geol* 17:197–207
- Sun S, McDonough WF (1989) Chemical and isotopic systematics of oceanic basalts: implications for mantle composition and processes. *Geol Soc Lond Special Publ* 42:313–345
- Taylor SR, McLennan SM (1985) The continental crust: its composition and evolution. Blackwell, Oxford
- Taylor SR, Rudnick RL, McLennan SM, Eriksson KA (1986) Rare earth element patterns in Archean high-grade metasediments and their tectonic significance. *Geochim Cosmochim Acta* 50:2267–2279
- Tchameni R, Mezger K, Nsifa EN (1995) Archaean and early Proterozoic evolution of the Congo Craton (Southern Cameroon). *EUG VIII Terra Abstracts* 7:102
- Tchameni R, Mezger K, Nsifa NE, Pouclet A (2000) Late Archaean crustal evolution in the Congo Craton: evidence from the K-rich granitoids of the Ntem Complex, Southern Cameroon. *J Afr Earth Sc* 30:133–147
- Teutsong T, Temga JP, Enyegue AA, Feuwo NN, Bitom D (2020) Petrographic and geochemical characterization of weathered materials developed on BIF from the Mamelles iron ore deposit in the Nyong unit, South-West Cameroon. *Acta Geochim* 40:163–175
- Toteu SF, Van Schmus WR, Penaye J, Nyobé JB (1994) U-Pb and Sm/N evidence for Eburnian and Pan-African high-grade metamorphism in cratonic rocks of southern Cameroon. *Precambrian Res* 67:321–347
- Toteu SF, Yongue RF, Penaye J, Tchakounte J, Seme Mouangue AC, Van Schmus WR, Deloule E, Stendal H (2006) U-Pb dating of plutonic rocks involved in the nappe tectonic in southern Cameroon: consequence for the Pan-African orogenic evolution of the central African fold belt. *J Afr Earth Sc* 44:479–493
- Walter MJ (1998) Melting of garnet peridotite and the origin of komatiite and depleted lithosphere. *J Petrol* 39:29–60
- Werner F, Erlenkeuser H, Grafenstein UV, McLean S, Sarnthein M, Schauer U, Unsold G, Walger E, Wittstock R (1987) Sedimentary records of benthic processes. In: Seawater-sediment interactions in Coastal Waters. American Geophysical Union (AGU), pp 162–262
- Whitney DL, Evans BW (2010) Abbreviations for names of rock-forming minerals. *Am Mineral* 95:185–187
- Wilson M (1989) Igneous petrogenesis. Springer, London, pp 245–285
- Winchester JA, Floyd PA (1977) Geochemical discrimination of different magma series and their differentiation products using immobile elements. *Chem Geol* 20:325–343
- Wood DA, Joron JL, Treuil M, Norry M, Tarney J (1979) Elemental and Sr isotope variations in basic lavas from Iceland and the surrounding ocean floor. *Contrib Miner Petrol* 70:319–339
- Wu Y, Zheng Y (2004) Genesis of zircon and its constraints on interpretation of U-Pb age. *Chin Sci Bull* 49:1554–1569
- Xia Z, Du W, Xia M, Jiang C (2018) Crustal contamination and magmatic evolution of the Beishan basic-ultrabasic intrusion belt in the Beishan Terrane, northeastern Tarim Craton (NW China). *Geol J* 2:1–14
- Zhang DY, Zhang ZC, Encarnación J, Xue CJ, Duan SG, Zhao ZD, Liu JL (2012a) Petrogenesis of the Kekesai composite porphyry intrusion, western Tianshan, NW China, Implications for met-allogenesis, tectonic evolution and continental growth during Late Paleozoic time. In: *Lithos*, pp 146–147
- Zhang ZC, Kang JL, Kusky T, Santosh M, Huang H, Zhang DY, Zhu J (2012) Geochronology, geochemistry and petrogenesis of Neoproterozoic basalts from Sugetbrak, northwest Tarim block, China, implications for the onset of Rodinia supercontinent breakup. *Precambrian Res* 220–221:158–176
- Zhang ZC, Mahoney JJ, Mao JW, Wang FS (2006) Geochemistry of picritic and associated basalt flows of the western Emeishan flood basalt province, China. *J Petrol* 47(10):1997–2019
- Zhou MF, Zhao JH, Jiang CY, Gao JF, Wang W, Yang SH (2009) OIB-like, heterogeneous mantle sources of Permian basaltic magmatism in the western Tarim Basin, NW China: Implications for a possible Permian large igneous province. *Lithos* 113:583–594

Publisher's Note Springer Nature remains neutral with regard to jurisdictional claims in published maps and institutional affiliations.